

SUPPLEMENTARY INFORMATION

Deoxyribonucleic Acid-Encoded and Size-Defined π -Stacking of Perylene Diimides

Jeffrey Gorman,¹ Sarah R. E. Orsborne,¹ Akshay Sridhar,² Raj Pandya,¹ Peter Budden,¹ Alexander Ohmann,¹ Naitik A. Panjwani,³ Yun Liu,¹ Jake L. Greenfield,⁴ Simon Dowland,¹ Victor Gray,⁵ Seán T. J. Ryan,¹ Sara De Ornellas,⁶ Afaf H. El-Sagheer,⁶ Tom Brown,⁶ Jonathan R. Nitschke,⁴ Jan Behrends,³ Ulrich F. Keyser,¹ Akshay Rao,¹ Rosana Collepardo-Guevara,¹ Eugen Stulz,⁷ Richard H. Friend,^{1*} Florian Auras^{1*}

¹ Cavendish Laboratory, University of Cambridge, Cambridge, CB3 0HE, United Kingdom

² Department of Applied Physics, Science for Life Laboratory, KTH Royal Institute of Technology, 171 21 Solna, Sweden

³ Berlin Joint EPR Lab, Fachbereich Physik, Freie Universität Berlin, 14195 Berlin, Germany

⁴ Yusuf Hamied Department of Chemistry, University of Cambridge, Cambridge, CB2 1EW, United Kingdom

⁵ Department of Chemistry, Ångström Laboratory, Uppsala University, 751 20 Uppsala, Sweden

⁶ Department of Chemistry, University of Oxford, Oxford, OX1 3TA, United Kingdom

⁷ Department of Chemistry & Institute for Life Sciences, University of Southampton, Highfield, Southampton, SO17 1BJ, United Kingdom

* Email: rhf10@cam.ac.uk, fa355@cam.ac.uk

Table of contents

A	Materials and methods	2	I	Cyclic voltammetry	18
B	Synthesis of the PDI phosphoramidite	4	J	Triplet sensitisation	18
C	DNA sequence design	7	K	PDI triplet formation	19
D	Solid-phase oligonucleotide synthesis	8	L	No photoinduced CT	20
E	Polyacrylamide gel electrophoresis	9	M	Transient EPR spectroscopy	21
F	Temperature-dependent UV-vis	10	N	NMR spectra	25
G	Concentration-dependent UV-vis	11	O	References	30
H	Molecular Dynamics Simulations	13			

Abbreviations

Chemicals

cod	1,5-cyclooctadiene
Cp	cyclopentadienyl
DBN	1,5-diazabicyclo[4.3.0]non-5-ene
DCM	dichloromethane
DMAP	4-(dimethylamino)pyridine
DMF	<i>N,N</i> -dimethylformamide
DMSO	dimethyl sulfoxide
DMTr	4,4'-dimethoxytriphenylmethyl
ETT	5-(ethylthio)-1 <i>H</i> -tetrazole
Fc	ferrocene
PBS	phosphate-buffered saline
TBA	tetrabutylammonium
PTFE	poly(tetrafluoroethylene)

TFA	trifluoroacetic acid
TEAA	triethylammonium acetate
THF	tetrahydrofuran

Other

CT	charge transfer
eq.	equivalents
GSB	ground state bleach
nt	nucleotide
PIA	photoinduced absorption
r.t.	room temperature
SE	stimulated emission
SPOS	solid-phase oligonucleotide synthesis

A. Materials and methods

Reagents and solvents were obtained in high-purity grades from commercial suppliers and were, unless shipped under argon, degassed and saturated with argon or N₂ prior to use. Mesitylene and pinacolone were degassed, dried over CaH₂, and passed through a 0.45 μm PTFE filter before use. TBAPF₆ (TBA = ⁿBu₄N⁺) electrochemical grade was purchased from Sigma Aldrich and recrystallised three times from EtOH. Ferrocene, used as a reference in cyclic voltammetry studies, was sublimed and stored under argon.

Chemical syntheses were carried out in oven-dried glassware under an argon atmosphere unless otherwise stated. Reactions were followed by analytical thin layer chromatography on aluminium-backed silica gel plates (Merck, 60 Å, F₂₅₄.) and visualised with ultraviolet irradiation (λ_{max} = 254 or 365 nm) or permanganate staining. Flash chromatography purification was carried out with Acros Organics ultra-pure silica gel (60 Å, 40-60 μm) under a positive pressure of air.

The procedure for the **DNA synthesis** is described in Section D. Inert spacer and endcapping strands were purchased from IDT and diluted in PBS (20 mM phosphate buffer, 200 mM NaCl).

Nuclear magnetic resonance (NMR) spectra were recorded on Bruker Avance III HD spectrometers. Chemical shifts are expressed in parts per million (δ scale) and are calibrated using residual (undeuterated) solvent signals as an internal reference (¹H NMR: CDCl₃: 7.26, DMSO-*d*₆: 2.50; ¹³C NMR: CDCl₃: 77.2, DMSO-*d*₆: 39.5). Data for ¹H NMR spectra are reported in the following way: chemical shift (δ ppm) (multiplicity, coupling constant, integration). Multiplicities are reported as follows: s = singlet, d = doublet, t = triplet, q = quartet, p = quintet, m = multiplet, br = broad, or combinations thereof. ¹³C NMR assignments were supported by DEPT-135 spectra where necessary.

Infrared (IR) spectra were recorded on Thermo Scientific Nicolet iN10, Perkin-Elmer Spectrum One, and Perkin-Elmer Spectrum BX FT-IR spectrometers equipped with attenuated total reflectance (ATR) units, with internal reference.

High resolution mass spectrometry (HRMS) was carried out using Bruker ultrafleXtreme matrix-assisted laser desorption/ionization - time of flight (MALDI-TOF) or Waters LCT Premier electrospray ionisation (ESI) mass spectrometers. Reported mass values are within the error limits of ± 5 ppm.

The experimental setup for **cyclic voltammetry (CV)** consisted of a polished glassy carbon working electrode, a Pt wire auxiliary electrode and an Ag wire quasi-reference electrode. All measurements were performed under an argon atmosphere and were referenced to ferrocene (Fc/Fc⁺) as an internal standard. A 0.1 M TBAPF₆/CH₂Cl₂ electrolyte was employed in the CV measurements.

Steady-state **UV-vis absorption spectra** were recorded on Perkin-Elmer Lambda 950, ThermoFisher NanoDrop ND-1000, or Agilent Cary 400 spectrometers.

UV-vis spectroelectrochemistry was performed using a BioLogic SP-150 potentiostat, an Agilent Cary 60 UV-Vis spectrophotometer, and an optically transparent thin layer electrochemical (OTTLE) cell (purchased from Spectroelectrochemistry Reading). The OTTLE cell comprised of a Pt gauze working electrode, a Pt wire counter electrode and an Ag wire reference electrode. A 0.5 M TBAPF₆/DMF electrolyte was employed in these studies. Measurements were performed at 298 K. Samples were prepared in the absence of oxygen and water and sealed in the sample chamber with PTFE plugs.

Steady-state photoluminescence (PL) emission spectra were recorded on an Edinburgh Instruments FLS980 spectrometer equipped with a photon counting PMT detector.

Photoluminescence Quantum Efficiencies (ϕ_F , PLQE) measure the ratio of photons emitted to photons absorbed by a sample. To measure the total yield samples are excited inside an integrating sphere. The ϕ_F values were determined by using the method from De Mello *et al.*^[1] Temperature and current controlled laser diodes (Thorlabs) were used to generate stable laser beams. These were focused through a small hole onto samples suspended in a Spectralon-coated integrating sphere (Newport 819C-SL-5.3) modified with a custom baffle extension. Light from the experiment was collected using an optical fibre connected to a Andor Kymera 328i spectrometer housing a DU490A-1.7 InGaAs detector.

For **femto-/picosecond transient absorption spectroscopy (fs-TAS)**, measurements were taken using a Pharos amplifier from Light Conversion (1030 nm, 190 fs, 38 kHz). The pump was the ~ 250 fs 530 nm output of an ORPHEUS optical parametric amplifier (Light Conversion), while the probe pulses were white light generated by a YAG crystal. Detection was read out by a custom camera (Entwicklungsbüro Stresing).

For **nanosecond transient absorption spectroscopy (ns-TAS)** measurements, the pump was generated by the output of a Ti:sapphire amplifier system (800 nm, 90 fs, 1 kHz, Solstice Ace), with a Light Conversion TOPAS to generate the desired pump wavelength. The probe was a ~1 ns pulse length supercontinuum laser (LEUKOS Disco STM-1-UV). The probe was split into a probe and reference beam to account for shot-to-shot fluctuations in the probe intensity. The probe and reference beams were focused into an imaging spectrometer (Andor, Shamrock SR 303i) and detected using a pair of linear InGaAs image sensors (Hamamatsu, G11608) driven and read out at the full laser repetition rate by a custom-built board (Entwicklungsbüro Stresing).

Time-dependent density functional theory (TD-DFT) and **transfer integral** calculations. The dimer structures from the MD simulations were used without further relaxation (without the DNA scaffolding). The excited states of the fragment chromophores were computed using TD-DFT within the Tamm-Dancoff approximation using ORCA (v4.2)^[2-3]. To account for the delocalized nature of the molecules, the CAM-B3LYP range-separated functional^[4] and def2-TZVP basis set^[5] were used in the calculations. The transfer integrals of the singlet excitation energy transfer (SEET) were then computed using the TrEsp method^[6-7] as implemented in Multiwfn^[8].

Transient electron paramagnetic resonance (trEPR) spectroscopy. Solutions of **PDI₁**, a modified **PDI₂** (without the T₇ inert strands) and **PDI₃** samples were prepared in a buffer/glycerol (80:20 by volume). The solutions were placed in fused silica EPR tubes, degassed via three freeze-pump-thaw cycles, and backfilled with helium to ca. 500 mbar. The samples were then flame sealed and stored at room temperature in the dark. Prior to the measurements, the samples were flash frozen in liquid nitrogen and placed in a pre-cooled (120 – 150 K) cryostat.

The trEPR experiments were performed on a laboratory-built X-band (9.7 GHz) continuous wave spectrometer together with a Bruker MD5 dielectric ring resonator with optical access. A 532 nm Nd:YAG pulsed laser (Atum Laser Titan AC compact 15 MM) with a 1 mJ, 5 ns length pulse operating at 100 Hz repetition rate was used to excite the sample in combination with a depolarizer to avoid polarization effects. The temperature was controlled using a temperature controller and helium flow cryostat, samples were measured at 100 K, 50 K and 10K. Transients were recorded as the static magnetic field was swept and continuous-wave microwave irradiation was applied (samples were measured at different microwave powers).

For analysis, EPR spectra were simulated using EasySpin.^[9]

B. Synthesis of the PDI phosphoramidite

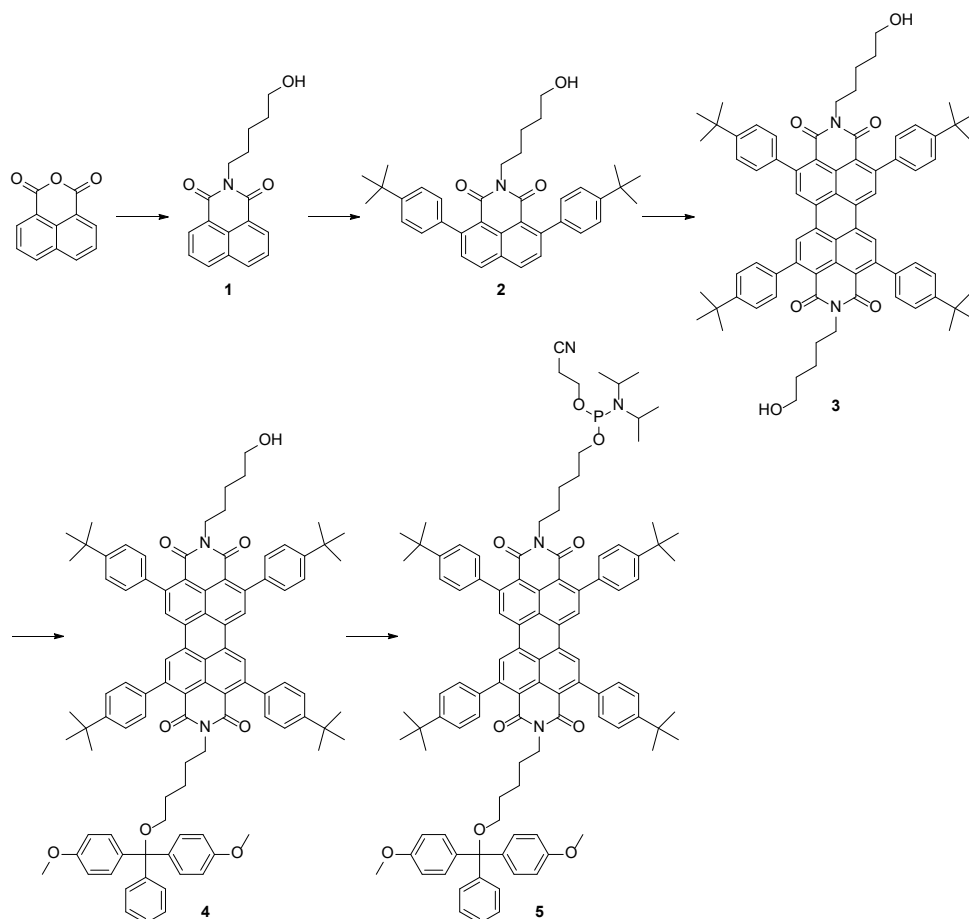
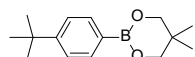


Figure S1. Synthesis of the perylene diimide (PDI) phosphoramidite.

4-*tert*-butylphenylboronic acid neopentyl glycol ester



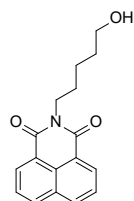
Adapted from literature.^[10] A reaction mixture containing 4-*tert*-butylphenylboronic acid (10.0 g, 56.2 mmol, 2.0 eq.), neopentyl glycol (9.00 g, 89.1 mmol, 1.6 eq.), MgSO₄ (6.0 g), and toluene (250 mL) was stirred in air at r.t. overnight. The crude was diluted with water (500 mL), and the product extracted with toluene (3 × 100 mL). The combined organic phases were washed with brine, dried over MgSO₄, filtered, and concentrated under reduced pressure to yield the title compound as a white solid (13.6 g, 55.1 mmol, 98 %).

¹H NMR (400 MHz, CDCl₃): δ 7.80 (d, *J* = 7.8 Hz, 2H), 7.44 (d, *J* = 8.0 Hz, 2H), 3.80 (s, 4H), 1.37 (s, 9H), 1.05 (s, 6H).

¹³C NMR (126 MHz, CDCl₃): δ 153.9, 133.9, 129.3 (br), 124.7, 72.4, 34.9, 32.0, 31.4, 22.0. The C-B signal is broad due to quadrupolar relaxation.

R_f = 0.86 (DCM).

Compound 1



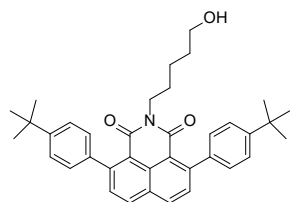
In accordance with literature.^[11] A suspension of 1,8-naphthalic anhydride (3.96 g, 20.0 mmol, 1.0 eq.) and 5-amino-1-pentanol (2.68 g, 26.0 mmol, 1.3 eq.) in absolute ethanol (90 mL) was heated under reflux for 4 h. The solvent was removed under reduced pressure and the residue was purified by column chromatography (silica gel, DCM/MeOH 100:1) to yield **1** as a white powder (6.45 g, 22.8 mmol, 91%).

¹H NMR (400 MHz, CDCl₃): δ 8.58 (dd, *J* = 7.2, 1.2 Hz, 2H), 8.19 (dd, *J* = 8.2, 1.2 Hz, 2H), 7.74 (dd, *J* = 8.2, 7.3 Hz, 2H), 4.23 – 4.15 (m, 2H), 3.71 – 3.62 (m, 2H), 1.78 (p, *J* = 7.5 Hz, 2H), 1.72 – 1.60 (m, 2H), 1.56 – 1.44 (m, 2H).

¹³C NMR (100 MHz, CDCl₃): δ 164.4, 134.0, 131.7, 131.3, 128.3, 127.1, 122.8, 62.9, 40.4, 32.5, 28.0, 23.4.

R_f = 0.46 (DCM/MeOH 10:1).

Compound 2



Adapted from literature.^[12] In a N₂-filled glovebox, compound **1** (708 mg, 2.50 mmol, 1.0 eq.), 4-*tert*-butylphenylboronic acid neopentyl glycol ester (1.85 g, 7.50 mmol, 7.5 eq.), RuH₂(CO)(PPh₃)₃ (275 mg, 0.30 mmol, 0.3 eq.), mesitylene (3.13 mL), and pinacolone (3.13 mL) were mixed in a sealed tube and heated at 140 °C for 3 d. The solvent was removed in vacuo and the dark red-orange oily residue purified by column chromatography (silica gel, DCM/EtOAc 95:5). The product fractions were concentrated under reduced pressure, then

further purified by column chromatography (basic alumina, DCM/EtOAc 98:2), followed by recrystallization from DCM/Heptane to yield **2** as light-yellow needles (985 mg, 1.8 mmol, 72%).

¹H NMR (400 MHz, CDCl₃): δ 8.13 (d, *J* = 8.4 Hz, 2H), 7.56 (d, *J* = 8.4 Hz, 2H), 7.52 – 7.46 (m, 4H), 7.36 – 7.30 (m, 4H), 4.04 – 3.95 (m, 2H), 3.58 (t, *J* = 6.5 Hz, 2H), 1.67 – 1.59 (m, 2H), 1.58 – 1.50 (m, 2H), 1.41 (s, 18H), 1.40 – 1.28 (m, 2H).

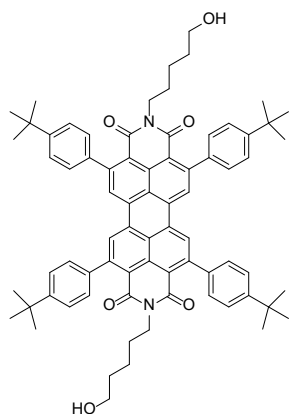
¹³C NMR (100 MHz, CDCl₃): δ 163.6, 150.3, 148.5, 139.9, 132.7, 132.0, 130.5, 130.0, 128.0, 125.2, 119.7, 63.0, 40.3, 34.8, 32.6, 31.6, 27.9, 23.3.

R_f = 0.73 (DCM/EtOAc 9:1).

FT-IR (ATR): ν = 3449 (br w, O-H), 2955 (m, C-H), 2867 (w, C-H), 1699 (s, C=O), 1660 (s, C=O), 1543 (w), 1498 (w), 1362 (s), 1316 (w), 1186 (m) cm⁻¹.

HRMS (ESI): *m/z* = 548.3140 [M + H]⁺; calculated for C₃₇H₄₂NO₃⁺: 548.3159.

Compound 3



Adapted from literature.^[13] tBuOK (3.02 g, 26.9 mmol, 6.0 eq.), DBN (4432 μL, 35.9 mmol, 8.0 eq.), and anhydrous toluene (40 mL) were mixed under argon and heated at 120 °C for 20 mins. In a separate flask, compound **2** (2.49 g, 4.50 mmol, 1.0 eq.) was dissolved in toluene (15 mL) under argon at 65 °C before cannula transfer into the hot tBuOK/DBN mixture. The resulting mixture was stirred for 3 h at 120 °C forming a dark blue solution. The reaction mixture was cooled to 80 °C and 2M aqueous HCl (15 mL) was added dropwise under vigorous stirring under argon. The intermediate was oxidised by halting the argon flow and slowly introducing air using an aspirator bulb, forming a bright red solution. The mixture was cooled to r.t., diluted with H₂O (300 mL), and extracted with chloroform (3 × 150 mL). The combined organic phases were washed with brine, dried over MgSO₄, filtered, and concentrated under reduced pressure. The solid was purified by column chromatography (silica gel, DCM/EtOAc

9:1) and triturated in DCM/MeOH to yield the title compound as a red powder (1.72 g, 1.59 mmol, 73 %).

¹H NMR (400 MHz, CDCl₃): δ 8.36 (s, 4H), 7.54 (d, *J* = 8.3 Hz, 8H), 7.38 (d, *J* = 8.3 Hz, 8H), 3.99 (t, *J* = 7.6 Hz, 4H), 3.58 (t, *J* = 6.5 Hz, 4H), 1.71 – 1.59 (m, 4H), 1.55 (dt, *J* = 14.3, 6.4 Hz, 4H), 1.43 (s, 36H), 1.41 – 1.31 (m, 4H).

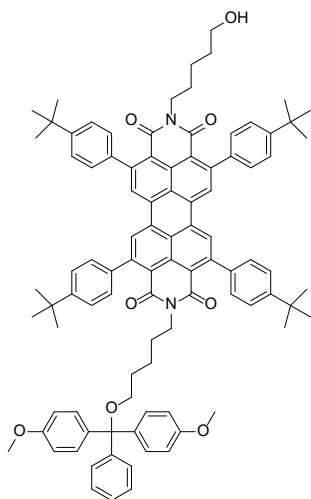
¹³C NMR (101 MHz, CDCl₃): δ 162.8, 150.7, 150.7, 148.7, 139.7, 132.9, 131.5, 128.2, 127.8, 125.5, 120.7, 63.0, 40.4, 34.9, 32.5, 31.6, 27.9, 23.3.

R_f = 0.45 (DCM/EtOAc 9:1).

FT-IR (ATR): ν = 3384 (br w, O-H), 2955 (m, C-H), 2861 (w, C-H), 1697 (s, C=O), 1661 (s, C=O), 1599 (m), 1538 (m), 1509 (m), 1434 (m), 1396 (m), 1337 (s), 1268 (m), 1202 (m), 1049 (w) cm⁻¹.

HRMS (MALDI-TOF): *m/z* = 1112.679 [M + Na]⁺; calculated for C₇₄H₇₇N₂O₆Na⁺: 1112.568.

Compound 4



A reaction mixture containing compound **3** (778 mg, 0.710 mmol, 1.0 eq.), DMAP (10 mg, 0.080 mmol, 0.11 eq.), anhydrous Et₃N (294 μL, 2.13 mmol, 3.0 eq.), and anhydrous DCM (75 mL) was stirred under argon at r.t. for 20 min. 4,4'-Dimethoxytrityl chloride (264 mg, 0.78 mmol, 1.1 eq.) was added as a solid in three portions over 1 h, against argon flow. The reaction was left to continue for another 2 h, quenched with MeOH (1 mL), and diluted with 75 mL of DCM. The organic phase was washed with sat. NaHCO₃, brine, dried over MgSO₄, filtered, and concentrated under reduced pressure. The solid was purified by column chromatography (silica gel, DCM/EtOAc/Et₃N gradient 90:10:3 – 50:50:3) and the second red band (containing **4**) was collected.

The first (bis-DMTr product) and third (starting material) red bands were collected and dried. The bis-DMTr product was converted back to the starting material by stirring in DCM/TFA (1:1 vol/vol) for 10 min. A red solid was precipitated by addition of MeCN, collected by filtration, washed with MeCN, and dried. The combined starting materials were subjected to reaction conditions and purification as above a further two times.

Finally, the combined fractions containing the desired mono-DMTr compound were concentrated under reduced pressure and triturated in DCM/MeOH to yield **4** as a red powder (624 mg, 0.45 mmol, 63 %).

¹H NMR (400 MHz, CDCl₃): δ 8.36 (s, 2H), 8.35 (s, 2H), 7.53 (d, *J* = 8.4 Hz, 4H), 7.50 (d, *J* = 8.5 Hz, 4H), 7.41 – 7.31 (m, 8H), 7.26 (d, *J* = 8.8 Hz, 4H), 7.21 (t, *J* = 7.4 Hz, 1H), 7.16 (d, *J* = 8.8 Hz, 2H), 6.82 (d, *J* = 8.8 Hz, 2H), 6.76 (d, *J* = 8.9 Hz, 4H), 3.97 (q, *J* = 8.3 Hz, 4H), 3.74 (s, 6H), 3.57 (t, *J* = 6.4 Hz, 2H), 2.96 (t, *J* = 6.9 Hz, 2H), 1.67 – 1.49 (m, 8H), 1.42 (s, 18H), 1.41 (s, 18H), 1.38 – 1.30 (m, 4H).

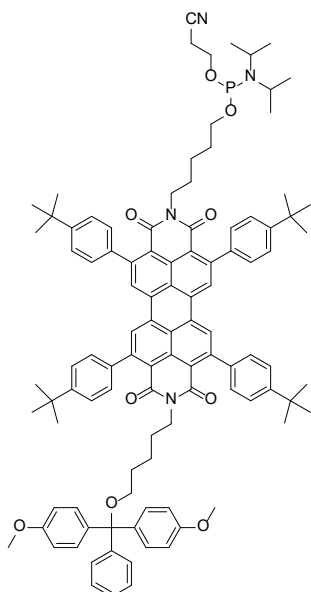
¹³C NMR (100 MHz, CDCl₃): δ 162.9, 162.8, 158.8, 158.4, 158.4, 150.7, 150.6, 148.7, 148.6, 145.5, 139.7, 139.6, 136.9, 132.9, 132.8, 131.5, 130.1, 129.3, 128.3, 128.3, 128.2, 128.0, 127.9, 127.2, 126.6, 125.5, 120.7, 120.6, 113.3, 113.1, 85.8, 81.6, 67.2, 63.5, 63.0, 55.4, 55.3, 40.6, 40.4, 34.9, 32.5, 31.6, 30.1, 27.9, 24.1, 23.3.

R_f = 0.69 (DCM/EtOAc 9:1).

FT-IR (ATR): ν = 2569 (br w, O-H), 2954 (m, C-H), 2860 (w, C-H), 1698 (s, C=O), 1665 (s, C=O), 1599 (m), 1542 (m), 1508 (m), 1435 (m), 1393 (m), 1365 (m), 1340 (s), 1270 (m), 1201 (m) cm⁻¹.

HRMS (MALDI-TOF): *m/z* = 1393.7224 [M]; calculated for C₉₅H₉₆N₂O₈: 1393.7239.

Compound 5



In an oven-dried, argon-filled round bottom flask with 4 Å molecular sieves, compound **4** (220 mg, 0.16 mmol, 1.0 eq.) was dissolved in anhydrous DCM (7 mL), followed by the addition of anhydrous *N,N*-diisopropylethylamine (111 μL, 0.64 mmol, 4.0 eq.). 2-cyanoethyl-*N,N*-diisopropylchlorophosphoramidite (105 μL, 0.47 mmol, 2.9 eq.) was added dropwise and the mixture was stirred gently at r.t. for 45 min. After completion, the solution was concentrated by an argon flow and precipitated with anhydrous MeCN (10 mL). The supernatant was removed under argon via a cannula with a filter tip until the solid residue was dry. The solids were washed with MeCN (10 mL) and the supernatant was again removed under argon via a cannula with a filter tip until the solid residue was dry. The solids were re-dissolved in anhydrous DCM (4 mL) and transferred to a thoroughly dried, argon-filled ampoule and used immediately for the oligonucleotide synthesis.

R_f = 0.53 (DCM/EtOAc 4:1).

Owing to the instability of this compound further characterisation was not achieved. Thorough exclusion of oxygen and water must be maintained throughout the synthesis and work-up.

C. DNA sequence design

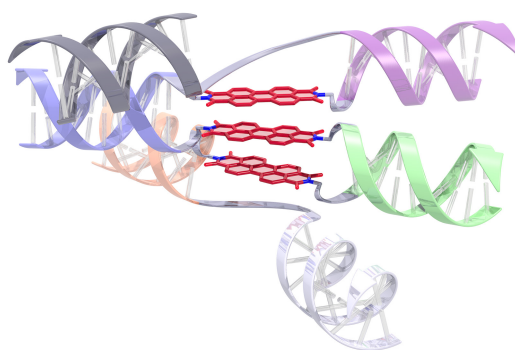


Figure S2. Schematic layout of the trimer **PDI₃**. Pairwise complementary DNA strands are colour coded.

The constructs discussed in this study are formed from seven (partially) complementary ssDNA strands. Each position within the constructs corresponds to two specific 11 nt sequences on either side of the cargo, which are complementary to their neighbouring strands – see base sequences below. Pairwise complementary DNA strands are colour coded. For each position, the desired cargo (PDI or T₇ inert spacer) can be chosen from cargo/DNA library.

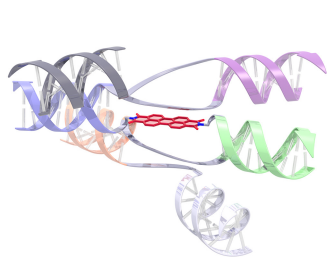
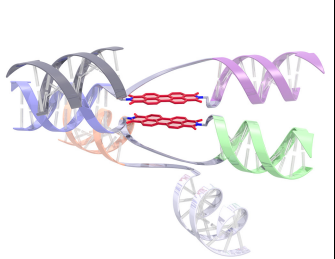
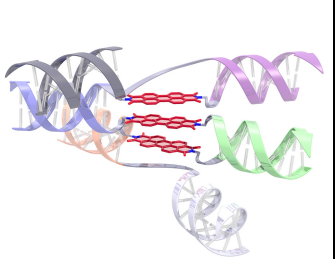
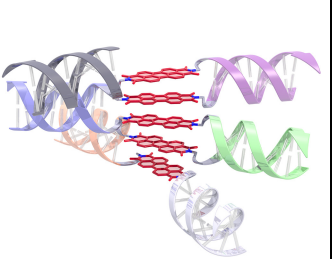
Table S1. Base sequences of the constructs. X = PDI cargo or T₇ spacer.

Position	Strand	Sequence
1	1	3' CTG GCT CAA TA 5'
2	2 _{PDI} or 2 _{T7}	5' GAC CGA GTT AT X TAA CCA GTG GA 3'
3	3 _{PDI} or 3 _{T7}	3' CAA GGC GGA TA X ATT GGT CAC CT 5'
4	4 _{PDI} or 4 _{T7}	5' GTT CCG CCT AT X ATT CTG TCT GG 3'
5	5 _{PDI} or 5 _{T7}	3' GGA CAT CCT TT X TAA GAC AGA CC 5'
6	6 _{PDI} or 6 _{T7}	5' CCT GTA GGA AA X TTA GGT GCA AG 3'
7	7	3' AAT CCA CGT TC 5'

Table S2. Base sequences of the individual strands.

Position	Strand	Sequence 5' -> 3'
1	1	5' ATA ACT CGG TC 3'
2	2 _{PDI}	5' GAC CGA GTT AT PDI TAA CCA GTG GA 3'
2	2 _{T7}	5' GAC CGA GTT ATT TTT TTT TAA CCA GTG GA 3'
3	3 _{PDI}	5' TCC ACT GGT TA PDI ATA GGC GGA AC 3'
3	3 _{T7}	5' TCC ACT GGT TAT TTT TTT ATA GGC GGA AC 3'
4	4 _{PDI}	5' GTT CCG CCT AT PDI ATT CTG TCT GG 3'
4	4 _{T7}	5' GTT CCG CCT ATT TTT TTT ATT CTG TCT GG 3'
5	5 _{PDI}	5' CCA GAC AGA AT PDI TTT CCT ACA GG 3'
5	5 _{T7}	5' CCA GAC AGA ATT TTT TTT TTT CCT ACA GG 3'
6	6 _{PDI}	5' CCT GTA GGA AA PDI TTA GGT GCA AG 3'
6	6 _{T7}	5' CCT GTA GGA AAT TTT TTT TTA GGT GCA AG 3'
7	7	5' CTT GCA CCT AA 3'

Table S3. Composition of the constructs discussed in this study.

			
Strands: 1 2 _{T7} 3 _{T7} 4 _{PDI} 5 _{T7} 6 _{T7} 7	Strands: 1 2 _{T7} 3 _{PDI} 4 _{PDI} 5 _{T7} 6 _{T7} 7	Strands: 1 2 _{T7} 3 _{PDI} 4 _{PDI} 5 _{PDI} 6 _{T7} 7	Strands: 1 2 _{PDI} 3 _{PDI} 4 _{PDI} 5 _{PDI} 6 _{PDI} 7

D. Solid-phase oligonucleotide synthesis (SPOS)

The oligonucleotides were synthesized trityl-on on solid supports (Glen Research, 1000 Å CPG) at a 1.0 μmol scale using standard protocols. The synthesis was carried out on an ABI 394 DNA/RNA Synthesizer in the standard mode, using 2-cyanoethyl-*N,N*-diisopropylphosphoramidites under inert conditions with anhydrous solvents.

For installing the semiconductor cargo, the 11-mer resin column (i.e., completed unmodified DNA segment) was transferred to an Expedite 8900 Nucleic Acid Synthesis System. First, the column was detritylated with deblock (3% trichloroacetic acid in DCM), followed by a MeCN wash. For the monomer coupling step, activator (0.25 M ETT in MeCN), semiconductor phosphoramidite **5** in DCM, and DCM were injected sequentially into the column in a 4:10:1 volume ratio, and coupled for 7 minutes with pulses of activator every 1 min to ensure a steady flow of fresh mixture. This cycle was repeated three times. The column was washed with DCM until the washings were colourless. The colour of the resin was inspected by eye to estimate semiconductor phosphoramidite coupling efficiency. If yields appeared poor the monomer coupling cycle was repeated. Sequential oxidation and capping steps were identical to standard DNA synthesis procedures.

The semiconductor-modified strands were transferred back to the ABI 392 Synthesizer, and an additional 11 DNA bases were coupled using standard DNA synthesis protocols.

The completed oligonucleotide solid phases were incubated in diethylamine for 30 min, washed with MeCN, and incubated overnight with 1 mL concentrated NH₄OH solution. The solutions were diluted by a factor of two with aqueous NaCl (100 mg mL⁻¹) and loaded onto Glen-Pack™ 60-5200-10 DNA purification cartridges (pre-washed with MeCN and TEAA), washed with brine, detritylated with 2% TFA, washed with H₂O, and eluted in MeCN/H₂O (1:1). The resulting red solutions were lyophilized. DNA conjugates were confirmed by mass spectrometry using MALDI-MS or ESI-TOF.

Table S4. Masses of semiconductor-ssDNA strands.

Strand	Mass expected	Mass found
2 _{PDI}	7979.0	7978.9
3 _{PDI}	7924.7	7924.9
5 _{PDI}	7990.0	7989.3
6 _{PDI}	7939.0	7939.9

E. Polyacrylamide gel electrophoresis (PAGE)

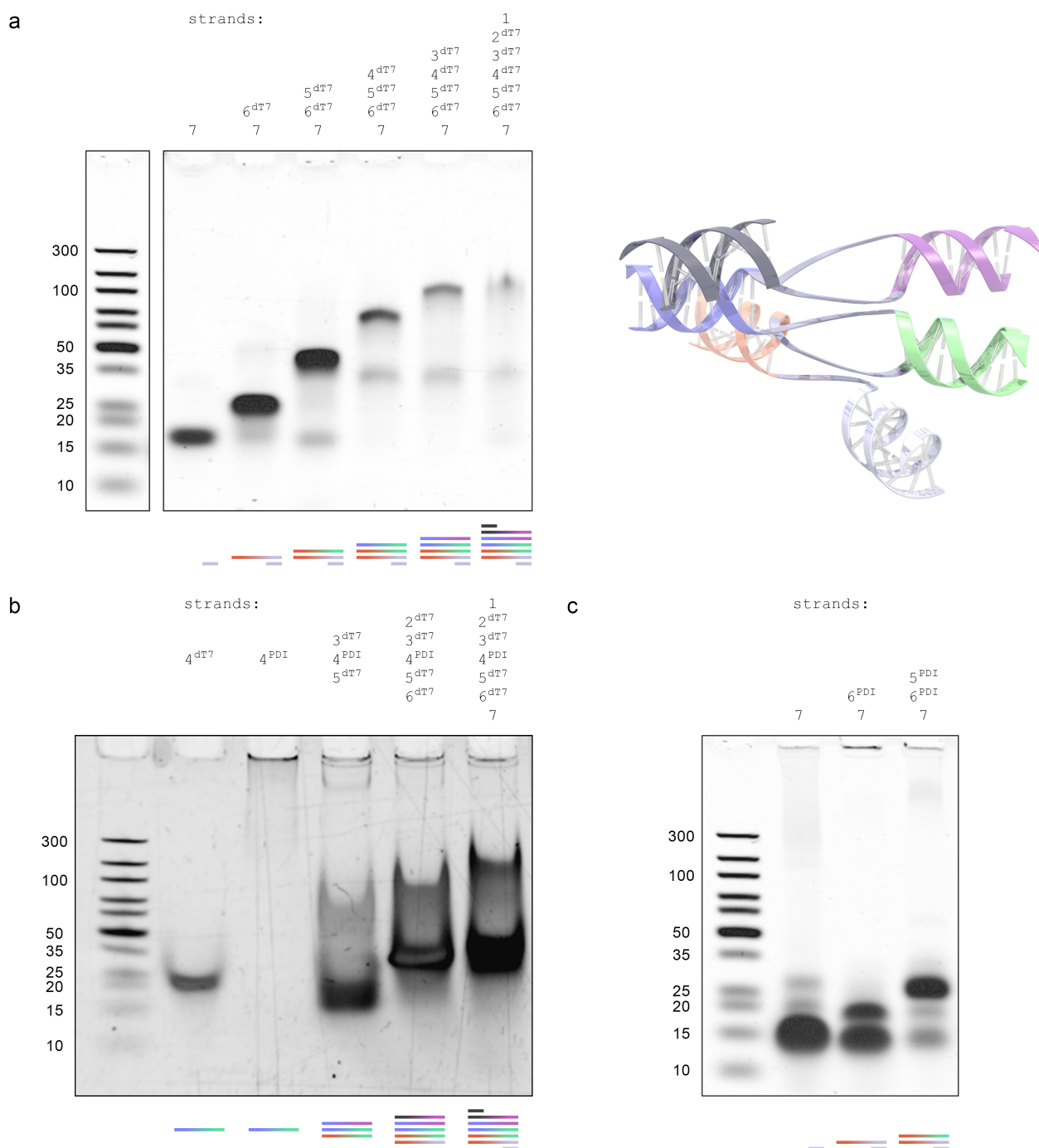


Figure S3. PAGE of DNA/cargo constructs.

(a) 10% Native-PAGE of reference constructs containing only the T₇ inert cargo. 100 V, 0 °C, 90 mins. Lane 1 is an Ultra Low Range DNA Ladder (10-300 base pairs) as a reference. The individual constructs are indicated at the top and bottom (colour coding is the same as the illustration on the right).

(b) 10% Native-PAGE of PDI₁. 100 V, 25 °C, 90 mins. Lane 1 is an Ultra Low Range DNA Ladder 10-300bp. Lane 2 (strand 4_{T7}) and lane 3 (strand 4_{PDI}) have the same nucleotide sequence, but with different cargo. 4_{PDI} (i.e. “monomeric” PDI) cannot permeate through the gel due to its hydrophobic core and aggregation. We can, however, track the assembly by flanking the PDI with T₇ inert cargo strands. Band streaking is a result of the perylene core. Lane 4 migrates faster than lane 2 despite more dsDNA due to the non-natural semiconductor cargo.

(c) 10% Native-PAGE of an unprotected PDI dimer. 100 V, 0 °C, 90 mins. Lane 1 Ultra Low Range DNA Ladder 10-300bp.

F. Temperature-dependent UV-vis spectroscopy

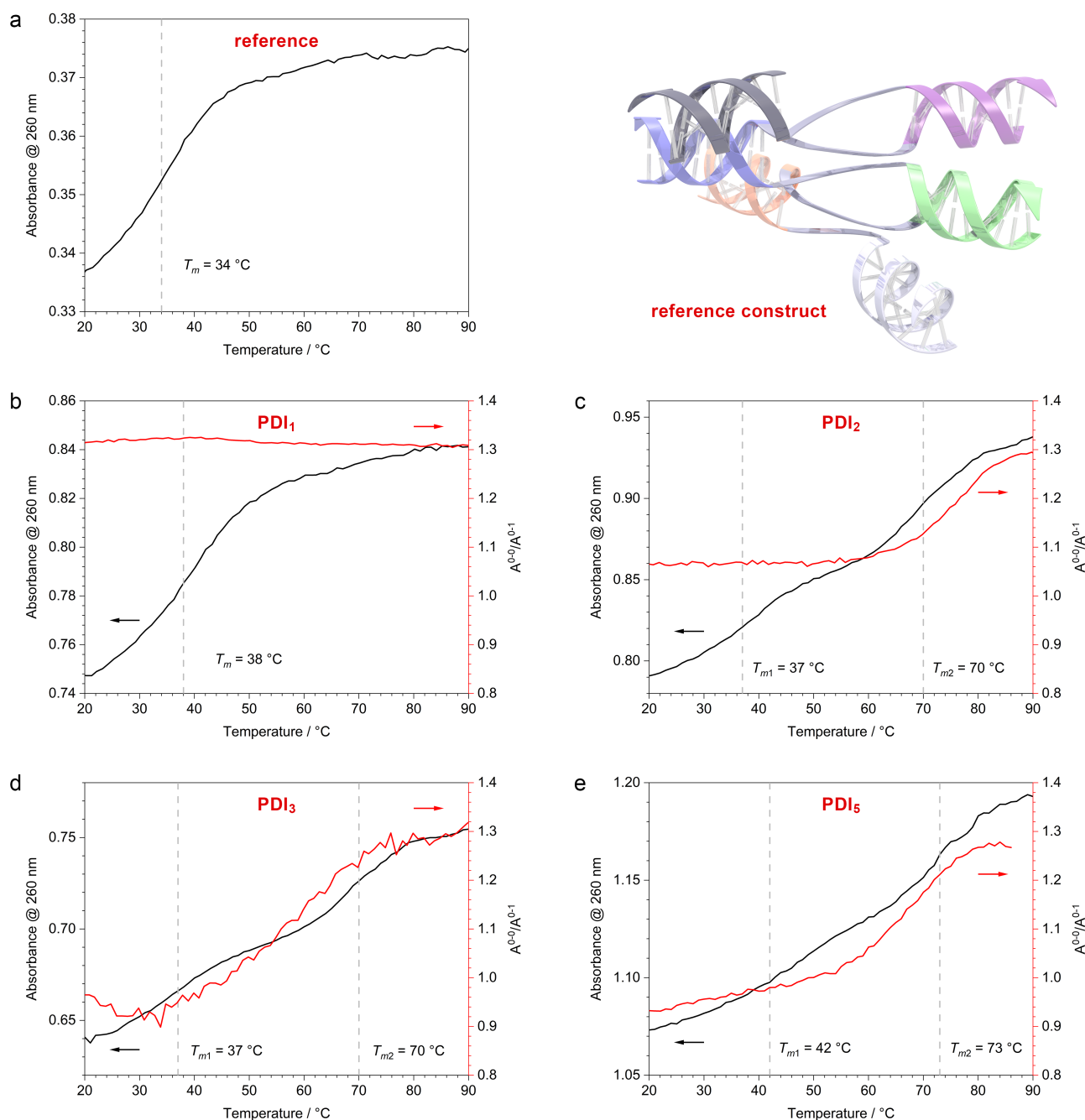


Figure S4. Thermal denaturing of the DNA constructs. The absorbance at $\lambda = 260\text{ nm}$ (black line, left y-axis) is used to monitor the loss of DNA hybridisation, while the A^{0-0}/A^{0-1} peak ratio (red line, right y-axis) of the vibronic bands tracks the disaggregation of the PDIs with increasing temperature.

(a) The reference construct containing five T₇ inert cargo (shown on the right).

(b) **PDI₁**. The melting temperature (T_m) is slightly higher, most likely due to the rigid PDI in the centre. A^{0-0}/A^{0-1} is relatively temperature-independent, as expected for monomeric PDI.

(c) **PDI₂**. Due to two PDIs in adjacent positions in the stack, we observe two distinct DNA melting temperatures for the strands that are reinforced by the PDIs (T_{m2}) and the T₇-containing strands (T_{m1}). The PDI aggregation changes from H-aggregated ($A^{0-0}/A^{0-1} \approx 1.05$) to quasi-monomeric ($A^{0-0}/A^{0-1} \approx 1.3$) upon melting of the PDI-containing strands around T_{m2} .

(d) **PDI₃**. The melting temperatures are very similar to PDI₂.

(e) **PDI₅**. Melting temperatures are broadened due to slightly different environments in the centre and the top/bottom of the stacks. Importantly, T_{m1} remains higher than T_m of the reference construct, confirming that PDI incorporation does not disrupt the DNA hybridisation.

G. Concentration-dependent UV-vis spectroscopy

There is a clear difference between a DNA/PDI conjugate with or without the inert T₇ strands. Single-stranded 3_{PDI} (Figure S5-1a) has no steric or Columbic protection of the hydrophobic perylene core and at higher concentrations is aggregated, as evidenced by vibronic peak ratio (A^{0-0}/A^{0-1}) of < 1. Upon dilution, a change in vibronic shift is observed as strand 3_{PDI} disaggregates, returning to a “monomeric” PDI spectrum. The changes in these vibronic peaks can be easily followed in the normalized data. In contrast, **PDI₁** retains the same “monomeric” PDI spectral features through the concentration assay (Figure S5-1b). The higher-order DNA-assembled PDI constructs **PDI₂**, **PDI₃**, and **PDI₅** are able to retain the same UV-vis spectra over the entire assay range. This indicates the assembly of our PDIs templates the formation of controlled aggregates composed of an exactly defined number of interacting semiconductors, a goal that is hardly achievable by aggregate formation via amphiphilic contrast.

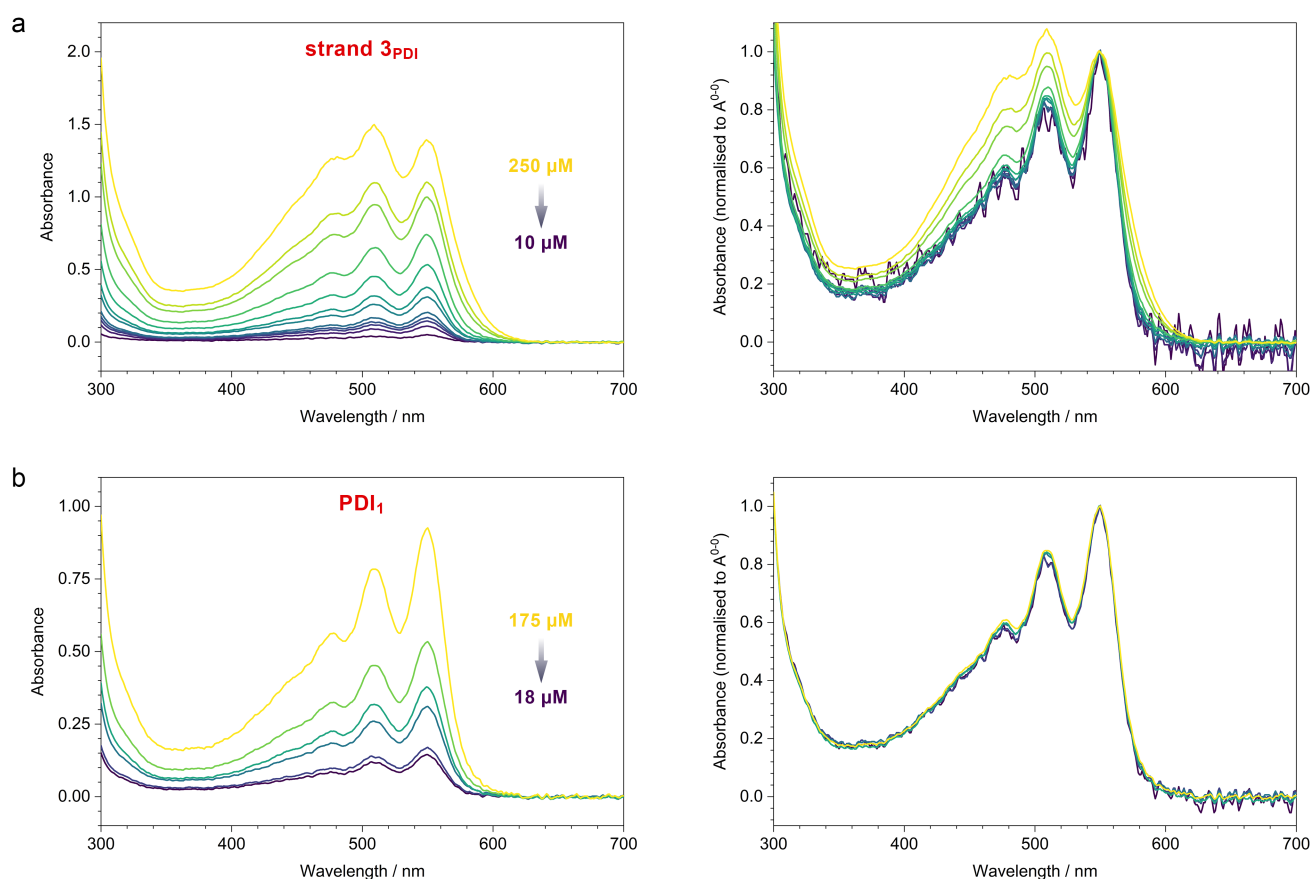


Figure S5-1. Concentration-dependent absorption spectra (left) and the spectra normalised to the absorbance of the 0-0 vibronic transition (right). All constructs are in PBS (20mM phosphate buffer, 200mM NaCl).

(a) Strand 3_{PDI} without the hybridised T₇ inert strands. The relative intensities of the vibronic bands change, indicating H-aggregation at higher concentrations.

(b) The assembled **PDI₁** with one PDI flanked by two T₇ inert strands on either side. The normalised spectra are virtually identical and monomer-like, indicating fully disaggregated PDIs.

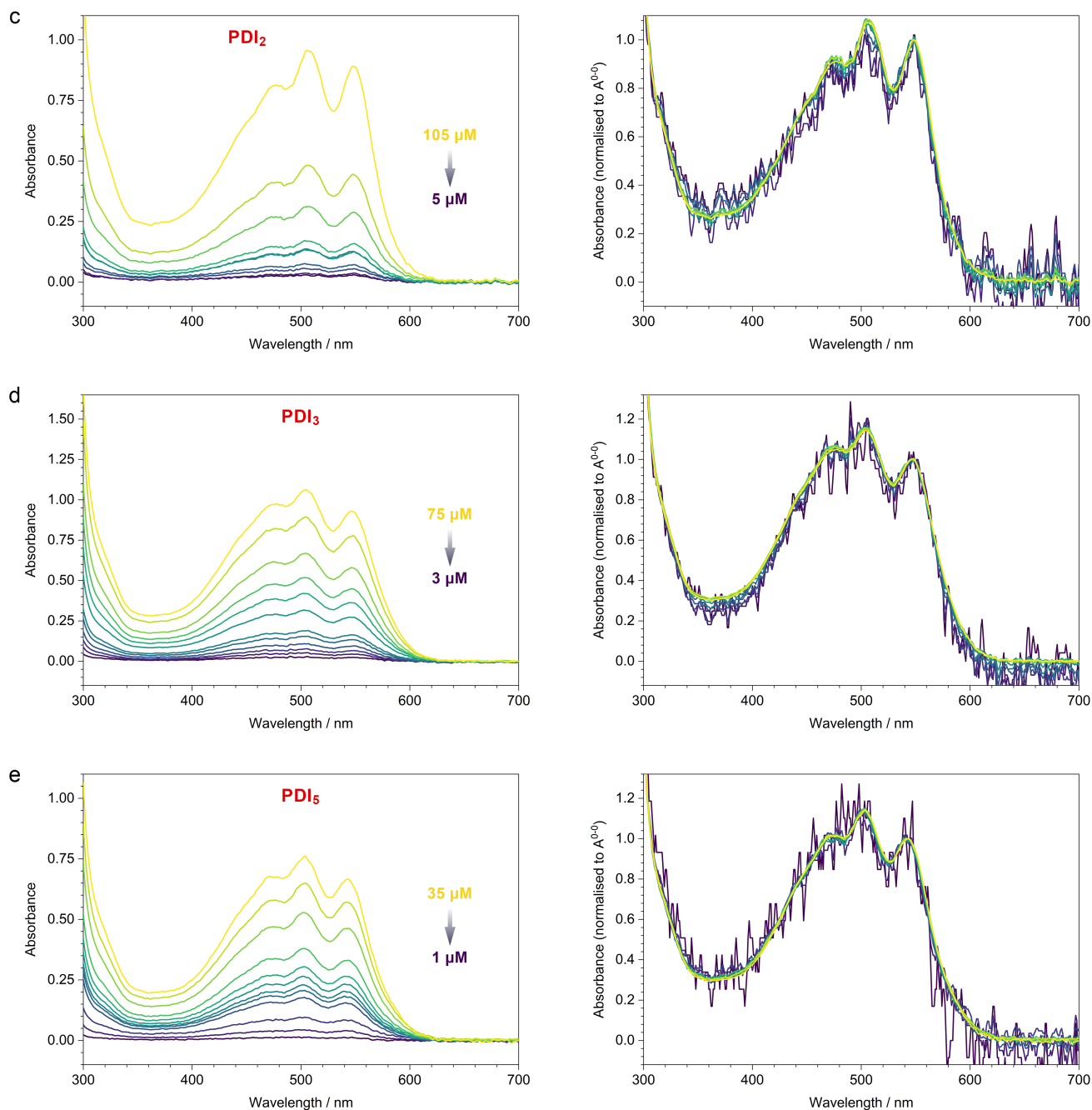


Figure S5-2. Concentration-dependent absorption spectra (left) and the spectra normalised to the absorbance of the 0-0 vibronic transition (right). All constructs are in PBS (20mM phosphate buffer, 200mM NaCl).

(c) The dimeric **PDI₂**. While there is the expected H-aggregation between the two PDIs inside the constructs, there is no sign of any additional aggregation across neighbouring constructs, confirming that the dyes are well shielded by the DNA shell.

(d) **PDI₃**. Similar to **PDI₂**, with strong H-aggregation inside the constructs but no additional concentration-dependent spectral changes.

(e) **PDI₅**. Similar to **PDI₂**, with strong H-aggregation inside the constructs but no additional concentration-dependent spectral changes.

H. Atomistic Metadynamics Molecular Dynamics Simulations

Parameterisation

For the PDI cargo, the semiconductor core and linkers were parameterised independently (Figure S6-1). The structures were generated using Marvin. Methyl capping groups were used for the PDI core. In the case of the linkers, acetyl and PO_3CH_3 capping groups were used. Hydrogen atoms were added to sketched molecules using Chimera.^[14] The PyRED server^[15] was used to calculate the electrostatic potential of the structures at the HF/6-31G* level of theory using Gaussian09, and then perform a two-stage Restrained Electrostatic Potential (RESP) fit^[16] to calculate the atomic charges. During the RESP fit, the partial atomic charges of the capping groups (Ac/Me/ PO_3CH_3) were restrained to match their values in the ff99sb^[17-18] and parmbsc1^[19] parameter set. Antechamber^[20] was then used to assign atom types to the semiconductor/linkers according to the GAFF2^[21] parameter set.

The dsDNA strands were built as 6 base pairs long B-DNA using Avogadro^[22]. The xleap module of Amber16^[23] was then used to remove the capping groups and append the linkers and PDI core. The DNA strands were parameterized using the parmbsc1 parameters^[19]. The system was solvated in an octahedral box of TIP3P^[24] solvent and 0.15 M NaCl ions that used the parameters of Joung and Cheatham^[25]. Finally, the amber parameters were converted to Gromacs^[26] format using the Parmed^[27].

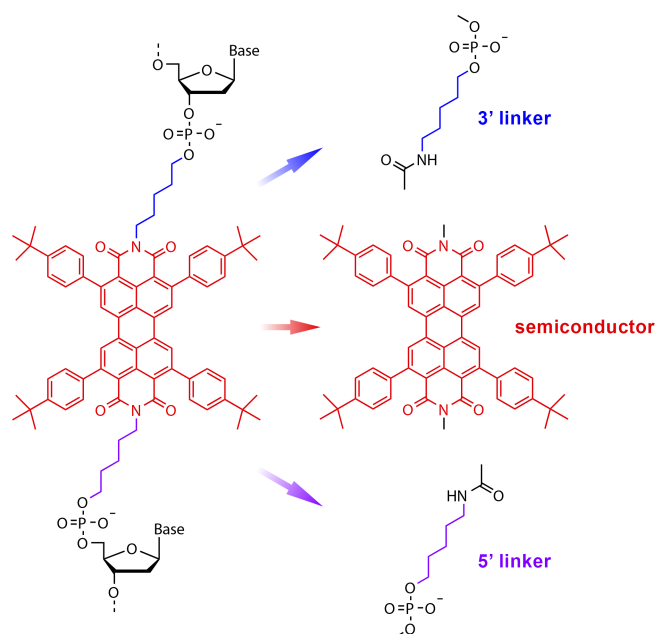


Figure S6-1. Parametrisation of the PDI cargo.

Simulation Setup

Models were first energy minimized until the maximum force on any of the atoms was below $1000 \text{ kJ mol}^{-1} \text{ nm}^{-1}$. The systems were then equilibrated using restraints on the DNA and semiconductors (force constants of $1000 \text{ kJ mol}^{-1} \text{ nm}^{-2}$) for 1 ns in the NVT ensemble followed by 1 ns in the NPT ensemble.

The simulations were performed starting with random velocities obtained from a Maxwell–Boltzmann distribution at 300 K and using a pressure of 1 bar. The temperature was kept constant using the V-rescale thermostat^[28]. The pressure was maintained using the Parrinello-Rahman barostat^[29]. Long-range electrostatics were calculated using the particle mesh Ewald (PME) algorithm^[30] with a cutoff of 1.0 nm. The simulations used a timestep of 2 fs and were performed using Gromacs 2020^[26] patched with Plumed 2.7.0^[31-32]. Trajectories were analysed using a combination of Gromacs and Plumed tools together with Python MDAnalysis scripts^[33].

Metadynamics Simulations

Following equilibration, for the PDI dimer, we performed well-tempered metadynamics simulations^[34-35], which use an external biasing potential to promote efficient sampling along chosen Collective Variables (ξ). The metadynamics biasing potential V_E used is constructed as a sum of gaussians deposited along the Collective Variable space (ξ_i) as:

$$V_E = \sum_{\{t=\tau_G, 2\tau_G, \dots\}} W \prod_i e^{\left(\frac{-(\xi_i - \xi_{ti})^2}{2\delta_i^2}\right)} \quad (1)$$

where τ_G is the time interval at which the gaussians are added with height W , width δ and mean ξ_{ti} . We used a two-dimensional gaussian ($i = 2$) to simultaneously bias the system along two important collective variables that determine the relative stacking orientations of the two semiconductors (Figure S6-2a). ξ_1 (also denoted as r) is defined as the Euclidean distance between the centres of the central aromatic rings of the two semiconductors. ξ_2 (also denoted as θ) is defined as the angle between two vectors identified by two pairs of atoms and is calculated as:

$$\theta = \xi_2 = \arccos\left(\frac{\vec{r}_{21} \cdot \vec{r}_{34}}{|\vec{r}_{21}| |\vec{r}_{34}|}\right) \quad (2)$$

where 1-2 and 3-4 are the terminal Nitrogen atoms of the two semiconductor molecules. However, it should be noted that, by definition, this ξ_2 includes the offset angle both along and orthogonal to the semiconductor molecule plane.

The metadynamics biasing potentials were deposited every 10 ps using a bias factor of 15 and gaussian widths of 0.008 nm and 0.025 radians along ξ_1 and ξ_2 respectively. The simulations were performed for 100 ns and convergence was assessed using the time-evolution of the free-energy profiles, which are invariant after ~ 50 ns (disregarding the time-dependant constant) (Figure S6-2b).

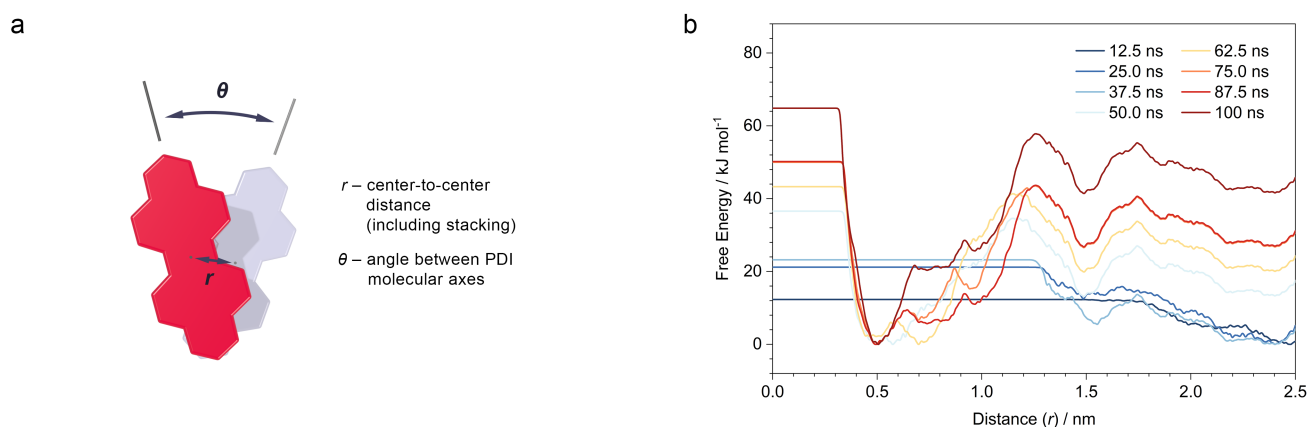


Figure S6-2. (a) Illustration of the distance and angle metadynamics collective variables. (b) Convergence of the PDI centre-to-centre distance.

Biased-Exchange Metadynamics Simulations

In simulations of the trimer, the energy landscape is multi-dimensional with stacking of two semiconductors in-turn influencing the other stacking interactions. Sampling the potential energy landscape of the trimer through standard well-tempered metadynamics (similar to the dimer) is thus computationally inexpedient with the requisite simulation time scaling exponentially.

The Bias-Exchange Metadynamics (BE-Metad) algorithm^[36] was thus used to simulate multiple replicas of the system in-parallel with each biasing a pair of PDI stacking as defined in Equation (1). At intervals of 10 ps, the configurations of two replicas i and j are swapped with an acceptance probability of

$$\min\left\{1, \exp\left[\left(\frac{1}{k_B T}\right) \left(V_E^i(r_i) + V_E^j(r_j) - V_E^i(r_j) - V_E^j(r_i)\right)\right]\right\} \quad (3)$$

where V_E^i is the history dependant bias of replica i . The trajectory of walkers thus traverse the landscape of each stacking interaction unencumbered by energy barriers along the other PDI stack. Similar to our prior work^[37], to allow a direct

averaging of system characteristics, an additional 'neutral' replica with no metadynamics biases ($V_E = 0$) was included in the BE-Metad simulations.

PDI dimer

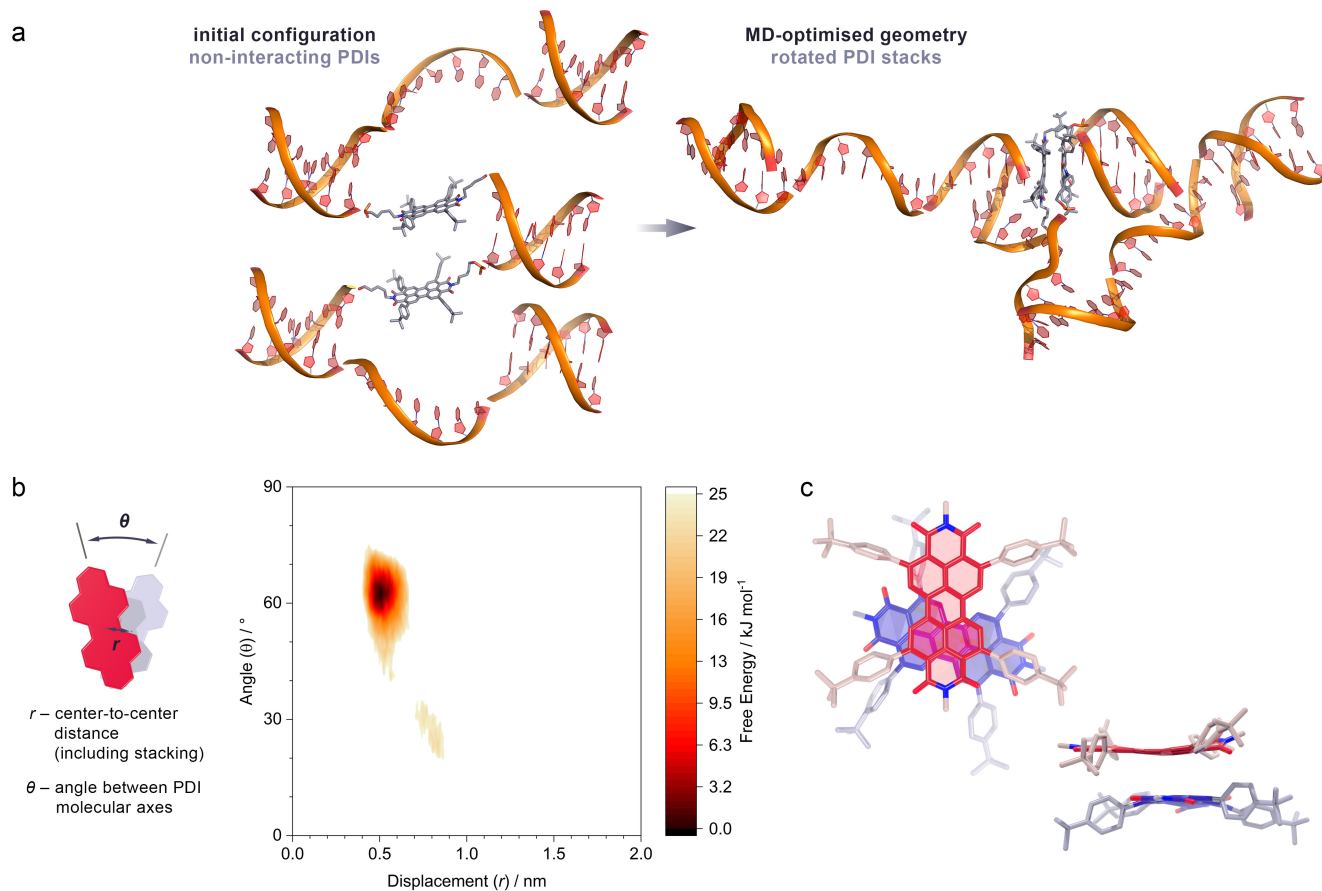


Figure S7-1. MD structure simulation of a PDI dimer flanked by two T₇ inert spacer cargos.

(a) Comparison of the initial (left) and the minimum-energy configuration (right).

(b) MD-calculated free energy maps probing the rotational offset θ and the centre-to-centre distance r between the PDIs. The energy scale is relative to the energy minimum. The PDI dimer has a well-defined energy minimum around $r = 0.5$ nm (i.e., π -stacked with only small lateral offset) and $\theta = 65^\circ$. This minimum is the same as the secondary minimum found for the PDI trimer. In the trimer, this geometry converts to the even more overlapping, slightly less rotated arrangement.

(c) The optimized PDI dimer consists of closely stacked PDIs that are rotated by about 65° . This configuration maximizes the overlap between the PDI cores while balancing the steric constraints due to the *tert*-butylphenyl units and the size mismatch between the dsDNA and the considerably smaller PDIs. Pentyl linkers and DNA are omitted for clarity.

PDI trimer

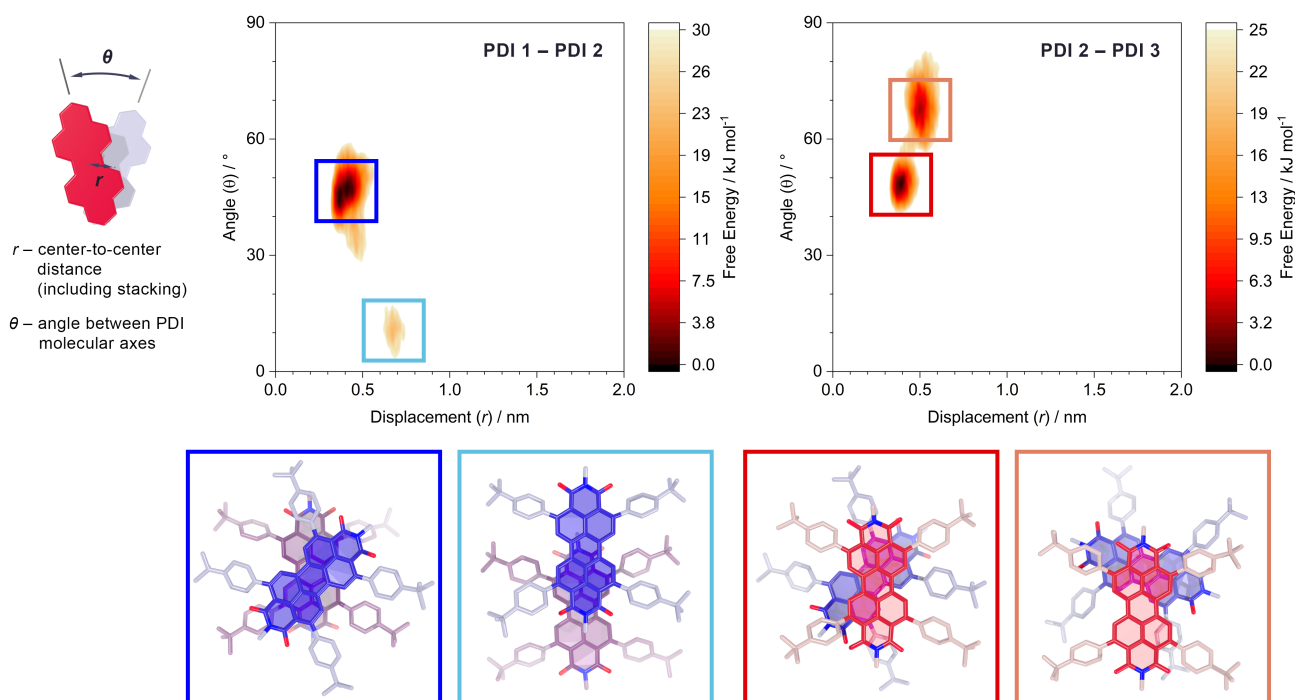


Figure S7-2. MD-calculated free energy maps probing the rotational offset θ and the centre-to-centre distance r between the neighbouring PDIs in the trimer. The energy scale is relative to the energy minimum. In addition to the global minimum around $r = 0.4$ nm and $\theta = 45^\circ$, each PDI pair has a secondary local minimum. These are different between the two PDI pairs because of the directionality of the DNA (PDI 1 is attached to the 5' end of the connecting dsDNA, whereas PDI 3 is connected to the 3' end). The geometries corresponding to the four minima are shown at the bottom. The local minimum of PDI 2 – PDI 3 (light red) is the same geometry as the minimum-energy configuration of the T₇-flanked dimer. This geometry converts into the stronger overlapping configuration (dark red) as the simulation proceeds.

PDI pentamer (PDI₅)

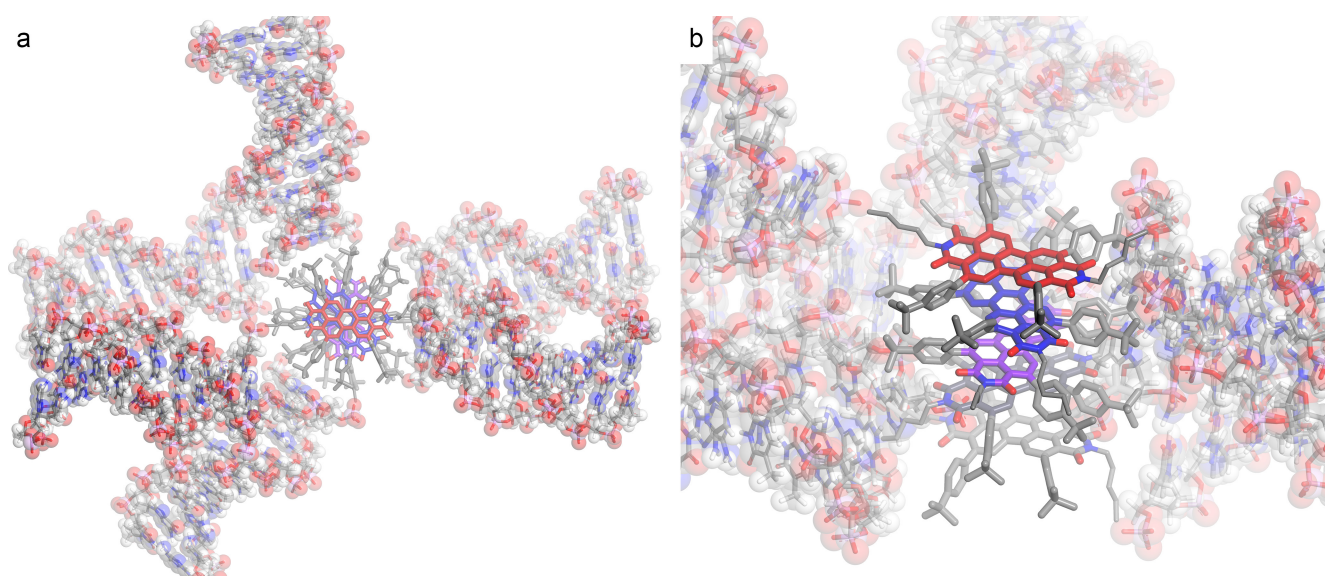


Figure 7-3. Force-field optimised model of PDI₅, viewed along the PDI stack (a) and rotated by 60° (b). While the pentamer is too large for the MD modelling techniques described above, this more cost-effective simulation technique allows to assess whether PDI stacks beyond a trimer are sterically feasible. The modelling confirms that the six bulky dsDNA of the PDI₅ can be distributed around a column of stacked PDIs. Like in the above PDI trimer, the PDIs in PDI₅ adopt a rotated stack configuration with a centre-to-centre distance of 0.4 nm and are rotated by 40 – 45° against their nearest neighbours. In contrast to the trimer, due to the increased steric constraints, we observe a clear preference for a screw-like packing motif with the rotation between adjacent PDIs in the same direction.

Impact of the dsDNA on the PDI packing

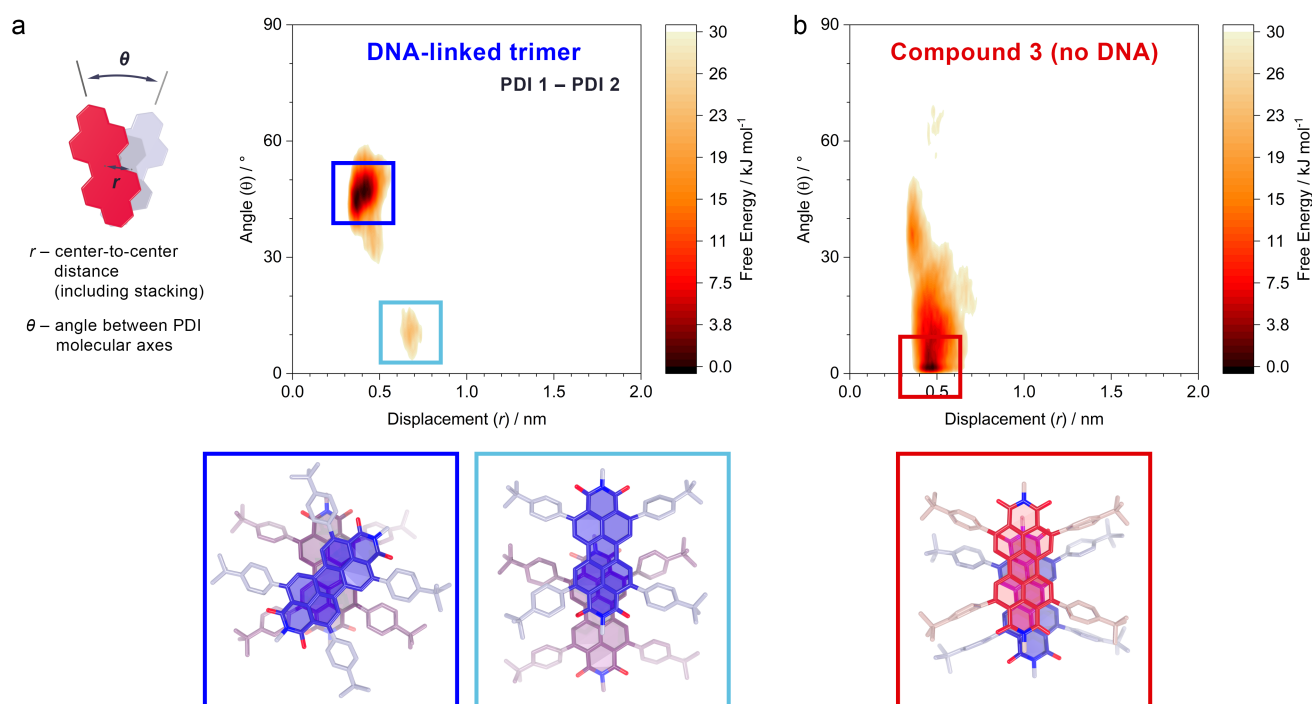


Figure S7-4. Influence of the DNA on the PDI packing (MD simulated structures). The PDI dimer geometries (bottom) correspond to the minima in the free energy maps (top). The energy scale is relative to the energy minimum.

(a) The DNA enforces the formation of rotated PDI stacks, while the slip-stacked arrangement that is commonly observed for *ortho*-functionalized PDIs is strongly disfavoured. The DNA and connecting alkyl chains are omitted for clarity.

(b) Without the DNA attached, the PDI diol **3** favours a slip-stacked arrangement that is similar to the solid-state structures of similar *ortho*-phenyl functionalised PDIs.^[38]

The potential for more extended structures

Can the assembly method developed in this study be used to create larger stacks? Since DNA is significantly larger (ca. 20 Å) than the π -stacking distance of PDIs (< 4 Å), the interconnecting dsDNA must be distributed radially around the PDIs. In order to analyse potential steric constraints, we simulated a PDI 10-mer stack using force-field methods. We found that even with the short pentyl connectors between the DNA and PDIs, the space around a central PDI column is sufficient. Thus, from a sterics perspective, there is no inherent upper limit to the size of the DNA/PDI constructs. In practice, the DNA hybridisation yield and/or solubility could limit the achievable construct size.

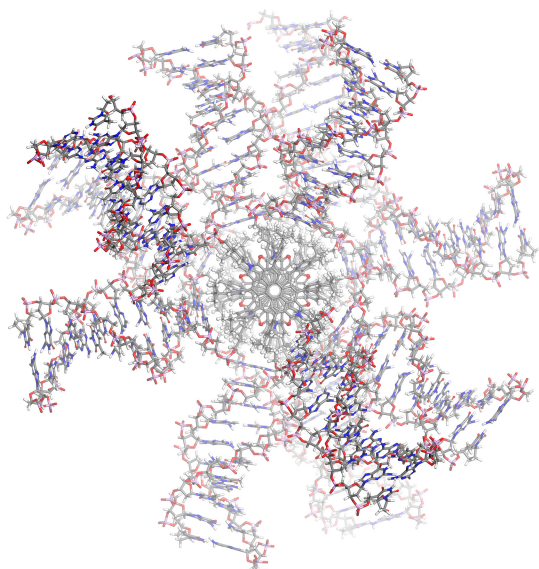


Figure S7-5. Force-field optimised model of a DNA-linked PDI 10-mer. The interconnecting and terminal dsDNA is distributed around the central PDI column without significant steric hindrance.

I. Cyclic voltammetry

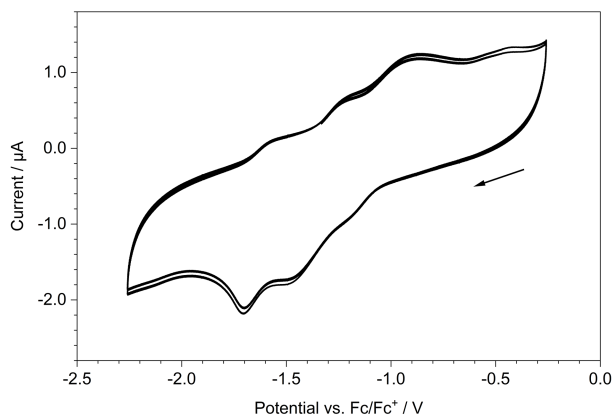


Figure S8. Cyclic voltammogram of the PDI diol **3**. Measured at 200 mV s^{-1} in a $0.1 \text{ M TBAPF}_6/\text{CH}_2\text{Cl}_2$ electrolyte under Ar. The arrow indicates the direction of the scan.

The oxidation of **3** diols is irreversible owing to the free hydroxyls, hence only reduction potentials were taken from the cyclic voltammograms. Lowest unoccupied molecular orbital (LUMO) energy levels were estimated using:

$$E_{LUMO} = -\left(4.8 \text{ eV} - E_{1/2}(\text{Fc}/\text{Fc}^+) + E_{\text{onset}}^{\text{red.}}\right)$$

Highest occupied molecular orbital (HOMO) levels were approximated by:

$$E_{HOMO} = E_{LUMO} - E_g^{\text{opt}}$$

Table S5. Estimated Frontier Molecular Orbitals.

	$E_{\text{onset}}^{\text{red.}} / \text{eV}$	E_{LUMO} / eV	$E_g^{\text{opt}} / \text{eV}^a$	E_{HOMO} / eV
PDI diol 3	-1.07	-3.73	2.25	-5.98

^a Determined from the absorption edge in $10 \mu\text{M}$ chloroform.

J. Triplet sensitisation

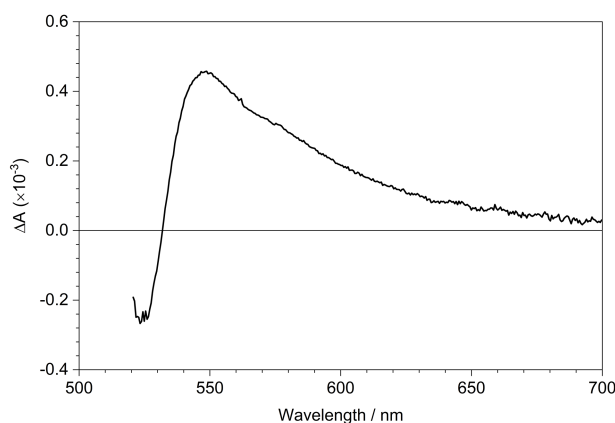


Figure S9. Photoinduced absorption spectrum of the PDI triplet. A $50 \mu\text{M}$ chloroform solution of the PDI diol **3** was sensitised with $100 \mu\text{M}$ anthracene. The spectrum is averaged over 50 - 400 μs after photoexcitation. $\lambda_{\text{excitation}} = 355 \text{ nm}$, $150 \mu\text{W}$ (150 nJ/pulse).

K. Supplementary note 1. PDI triplet formation

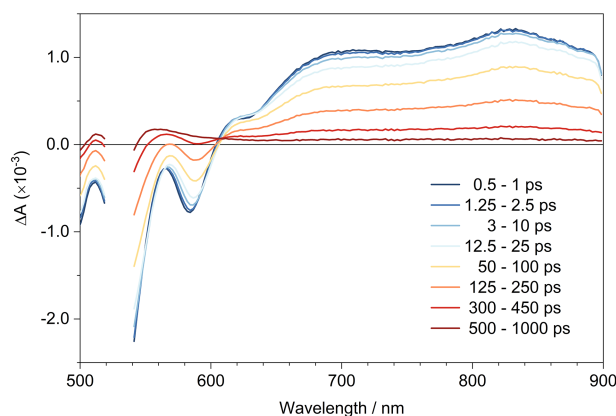


Figure S10. Femto-/picosecond transient absorption spectra of a solution of the PDI diol **3** in CHCl_3 ($12.5 \mu\text{M}$). $\lambda_{\text{excitation}} = 530 \text{ nm}$. 520 - 540 nm removed due to pump scatter.

fs-TA spectra were obtained for the reference diol **3** in dilute chloroform solutions ($< 20 \mu\text{M}$), excited at 400 nm. Following excitation, negative GSB and SE signals are observed centred at 535 nm and 580 nm respectively. Absorption bands centred at 675 and 915 nm are assigned to the PIA of the singlet excited state (^1PDI). ^1PDI decays monoexponentially with a lifetime of $171 \pm 5 \text{ ps}$. A new PIA at 550 – 575 nm persists for into the microsecond regime with a lifetime of 419 ns. This long-lived PIA feature has previously been identified in analogous compounds to the triplet PIA, ^3PDI .^[38-39] High dilution rules out singlet fission as the origin of the sub-ns triplet formation.

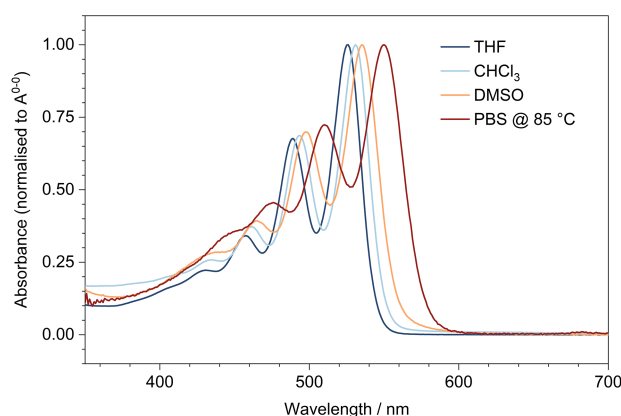


Figure S11. Normalised steady-state absorption of dilute PDI reference diol **3** in various solvents ($12.5 \mu\text{M}$). PDI-ssDNA (strand 4_{PDI}) in PBS (20 mM phosphate buffer, 200 mM NaCl) at 85°C for comparison.

Previous dilute ortho-arylated PDIs have formed triplets on short timescales from the charge-transfer between the electron-rich ortho-aryls and electron-poor perylene core.^[39-40] The charge-transfer character is observed by red-shifting solvatochromism between chloroform ($\epsilon = 5$), THF ($\epsilon = 8$), DMSO ($\epsilon = 47$).^[41] Furthermore, out-of-plane vibrations from the non-planar substituents have been suggested to mediate fast spin-orbital coupled intersystem-crossing.^[42] This fast triplet formation in the diol supports the low PL quantum efficiency ($\phi_{\text{F}} = 2.6\%$) of the molecule. Consistent with the out-of-plane vibrational argument, we observe an increase in PLQE if PDI diol **3** is immobilised in a solid matrix (0.1 wt-% in polystyrene; $\phi_{\text{F}} = 17.2\%$) or in pure drop-cast films ($\phi_{\text{F}} = 22.6\%$).

L. Supplementary note 2. No photoinduced charge transfer in the PDI/DNA constructs

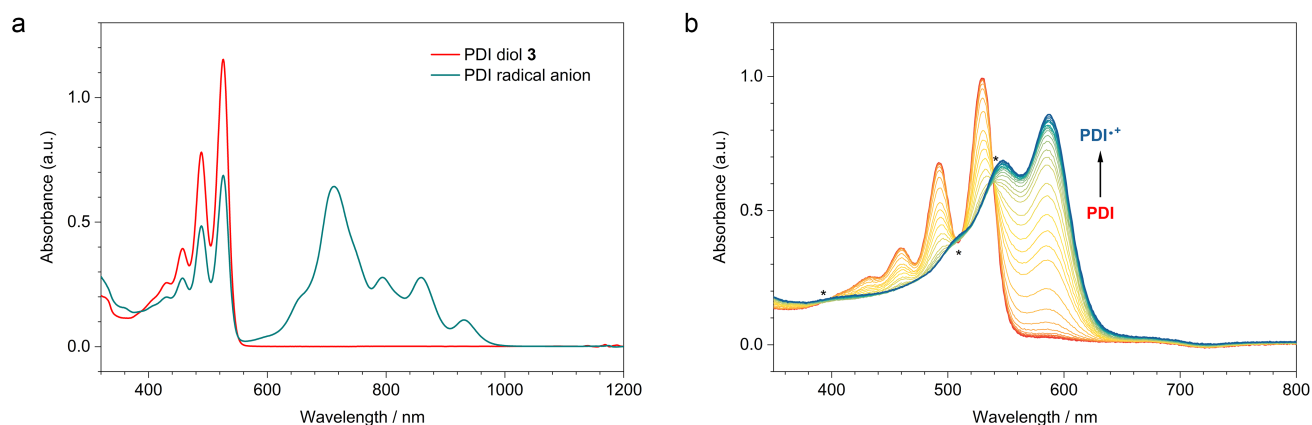


Figure S12. Absorption spectra of (a) the PDI radical anion and (b) radical cation.

(a) Absorption spectrum of the PDI diol **3** (red) and its radical anion (green) generated via chemical doping. PDI diol: 12.5 μM in degassed dry BHT-free THF. Anion: 12.5 μM PDI diol **3**, 12.5 μM CoCp₂ in degassed, dry BHT-free THF.

(b) Absorption spectrum of the PDI radical cation (blue) generated by electrochemical oxidation of the PDI diol **3** (red). Spectra are normalised to their integral. Solvent: dry CH₂Cl₂. The arrow indicates the progression of the spectra over the course of the oxidation. Isosbestic points are marked with asterisks, confirming the transformation between two species upon oxidation.

Previous PDI-DNA conjugates have observed hole-transfer to guanine and adenine upon PDI excitation, leaving a radical anion on the PDI (PDI^{-•}).^[43-47] Interestingly, we observe no PDI^{-•} PIA in our PDI/DNA constructs. The chemically generated radical anion of the PDI diol **3** has strong absorption in the 600 – 800 nm range with the strongest absorption band centred at 712 nm (Figure S13a), which should be clearly visible in the fs- and ns-TA data (Figure 4 and Figure S10) if there was any charge transfer to the DNA.

In contrast to most other PDI-DNA conjugates our molecules have a longer (pentyl) chain between the imide and first nucleotide, greater steric bulk of the four *tert*-butylphenyl groups, and a non- π -stacking orientation relative to the nucleobases. We note that our tetrasubstituted PDI singlet in chloroform is much shorter lived than unsubstituted PDIs. Based upon work on distance dependence of hole transfer in PDI-DNA hairpins by Wasielewski *et al.*, we have designed our base sequences with a minimum of three base pair separation between the PDI core and the nearest guanosine.^[44] This minimises the chance of hole transfer directly to guanine, or by superexchange via adenine. Taken together hole transfer to guanine is inhibited in our DNA/PDI constructs.

Furthermore, the high solvent dielectric constant of PBS ($\epsilon = 48$) and coupling between PDI semiconductors could produce radical cations and anions by symmetry-breaking charge-transfer (SBCT). As stated above, no radical anion is observed. We note the steady-state absorption of the PDI radical cation in CH₂Cl₂ is 550 – 600nm (Figure S13b). However, we observe no sharp features in the PDI₂, PDI₃, or PDI₅ PIAs that would suggest the formation of the PDI radical cation species.

We note the strong coupling between PDIs in PDI₂, PDI₃, and PDI₅ results in excimer formation (Figure S10) which is lower energy than the CT state in a strong-coupling regime. However, the excimer state does contain an admixture of CT-character, as opposed to “full CT” formation.^[48]

M. Transient EPR spectroscopy

The transient electron paramagnetic resonance (trEPR) spectra of **PDI₁**, a modified **PDI₂** (without the T7 inert strands), and **PDI₅** were measured each at three different temperatures (100 K, 50 K, 10 K) with excitation at 532 nm. Figure S14-1 shows the spectra measured with a microwave power of 7.9 μ W and recorded at 1.5 μ s delay after flash (DAF), which is when the triplet signal maximises. Figure S14-2 displays the same samples measured with a microwave power of 126 μ W and 0.9 μ s DAF, corresponding to the time when the triplet signal is maximal. The microwave power affects the transient kinetics with higher power giving transients approaching the T₂ spin-spin relaxation dynamics and less power giving transients decaying with the T₁ spin lattice relaxation or species lifetime dynamics. For data analysis, we fit the triplet spectra measured with a microwave power of 7.9 μ W at 1.5 μ s DAF, as these spectra are less affected by the Torrey oscillations induced by the higher microwave powers.

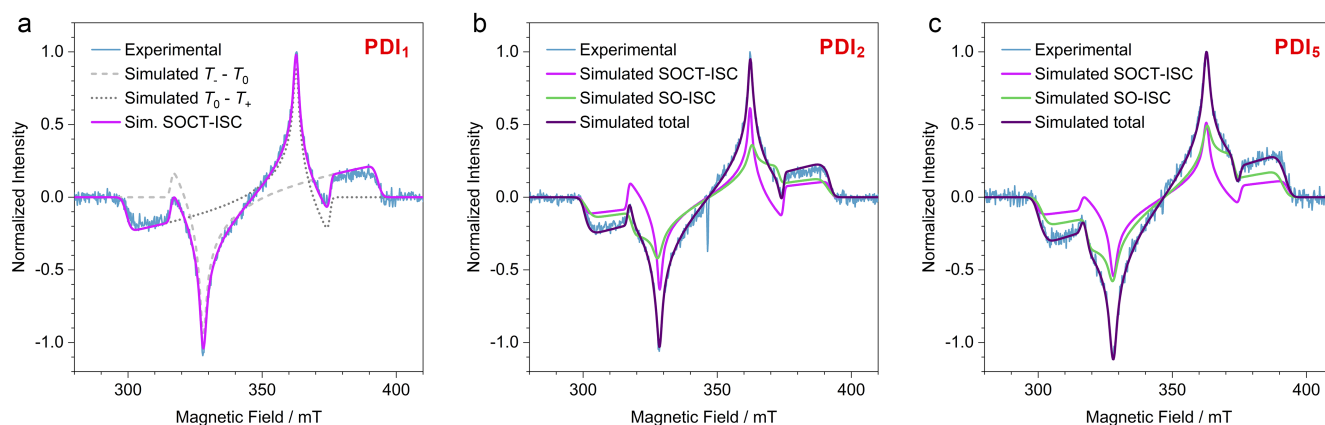


Figure S13. trEPR analysis of (a) **PDI₁** (same as main manuscript Figure 4, added here for comparison), (b) a modified **PDI₂** (without the T₇ inert strands), and (c) **PDI₅** (same as in main manuscript), recorded at 100 K, time averaged 0.5 – 4 μ s after optical excitation at 532 nm. For the modified **PDI₂**, the simulated spectrum (dark line) requires two triplet species with different ESP to match the experimental data. These species are a triplet formed via SOCT-ISC with an *ae/aea* ESP (61%; purple line) and a triplet due to an excimer-based SO-ISC with an *eee/aaa* ESP (39%; green line).

Table S6. Triplet state parameters obtained from simulation using EasySpin.^[9]

Sample	Triplet formation mechanism	ESP pattern	Population p_x, p_y, p_z	p_x/p_y ratio	D / MHz	E / MHz
PDI₁	SOCT-ISC (100%)	<i>ae/aea</i>	0.18, 0.82, 0	0.22	1314 (92*)	-115
	-/-					
PDI₂ (modified)	SOCT-ISC (61%)	<i>ae/aea</i>	0.06, 0.94, 0	0.06	1285 (64*)	-114
	excimer SO-ISC (39%)	<i>eee/aaa</i>	same as PDI₅ excimer SO-ISC			
PDI₅	SOCT-ISC (31%)	<i>ae/aea</i>	same as PDI₁ SOCT-ISC			
	excimer SO-ISC (69%)	<i>eee/aaa</i>	0.46, 0.54, 0	0.85	1260 (125*)	-93

* D strain, line broadening in MHz.

The **PDI₁** triplet spectrum can be simulated with a single triplet species (Figure S13a) with the zero-field splitting (ZFS) parameters and relative sublevel populations given in Table S6. The observed *ae/aea* electron spin polarization pattern (ESP) reveals a spin-orbit charge transfer intersystem crossing (SOCT-ISC) mechanism^[49-51] for the triplet formation, which is consistent with the known charge transfer (CT) character of ortho-phenyl substituted PDIs.^[12, 40]

In the case of **PDI₅**, the spectrum can only be simulated considering the contribution of two triplet species (Figure S13c). We anticipate the first species to be the same as for **PDI₁** (i.e., *ae/aea* ESP due to SOCT-ISC) with the parameters obtained from the simulation of **PDI₁**. The second triplet species has an *eee/aaa* ESP with smaller ZFS parameters,

suggesting a more delocalized triplet that originates from an excimer-based spin-orbit coupling mediated intersystem crossing (SO-ISC mechanism).^[52] In PDI₅, the excimer-based SO-ISC triplet formation dominates with a contribution of 69%, while the SOCT-ISC triplet contribution is 31%.

We also studied a modified PDI₂ without the T₇ inert strands on both sides of the PDI cargo (Figure S13b). Similar to PDI₅, the spectrum consists of two triplet species, but the overall triplet spectrum width (2D) is smaller than in PDI₁ and PDI₅. Thus, we cannot use the above simulation parameters from the PDI₁ and PDI₅ SOCT-ISC triplet for the data analysis. Instead, we fix the excimer-based SO-ISC triplet species using the parameters extracted for PDI₅ and fit the SOCT-ISC triplet species. The simulated spectrum provides a very good fit to the experimental data with the ZFS parameters and sublevel populations stated in Table S6. This confirms that the modified PDI₂ has indeed a contribution from a SOCT-ISC formed triplet state, albeit with a smaller *D* parameter than PDI₁ and PDI₅ but similar *E* value. This suggests a more delocalized SOCT-ISC triplet state in this sample with also more polarized triplet sublevels ($p_x/p_y = 0.06$ for PDI₂ vs. 0.22 for PDI₁ and PDI₅). The difference in the triplet sublevel populations and ZFS parameters for PDI₂ is most likely due to a less rigid structure and therefore slightly different conformations of the PDI molecules when frozen.

Overall, we observe a clear trend in the dominating triplet formation mechanism with increasing number of coupled PDIs per construct, from exclusively SOCT-ISC in PDI₁ to a dominant excimer-based SO-ISC contribution in PDI₅.

Charge transfer and temperature dependence of the trEPR signal

A charge transfer (CT) state (also known as a spin correlated radical pair) is a cation/anion pair which exhibits exchange and/or dipolar spin-spin interaction. This leads to a very specific signature in trEPR where an absorptive and emissive signal arises for each radical in the pair, resulting in four EPR transitions for the coupled radical pair.^[53-55] The observation of CT state signal requires weak coupling between the radicals and the coupling depends on the distance between the radicals. In the case of PDI₁ there is no apparent CT state signal in the trEPR, even at the lower temperature of 10 K, which suggests that the 2J coupling between the radicals is very large. In the strong coupling limit, i.e.,

$$\frac{1}{2}(g_A - g_B) \frac{\mu_B}{\hbar} B_0 \ll J + \frac{1}{2}d$$

no CT state signal can be observed in EPR. This, however, can therefore also mean that the large electronic coupling of the singlet CT (¹CT) state leads to direct SO-ISC to the ³PDI, i.e., the SOCT-ISC mechanism. On the other hand, in the case of PDI₅ there is a small CT signal at 100 K which becomes more apparent and increasingly symmetric in polarization (absorptive and emissive bands become more equal in intensity) at lower temperatures. Even at the lower temperatures, however, the signal intensity is much smaller than that of the triplet and suggests that the CT state is only a small contribution and a minor excitation pathway, attributed to the partial charge transfer character of the excimer.

The PDI₂ system also shows small CT signal at 100 K, which increases in intensity as the temperature is lowered. However, this time the signal intensity is as large as the most intense triplet peaks at 10 K. The polarization pattern of the CT state is the same in PDI₂ and PDI₅ and is of *a/e* polarization. In systems where the donor and acceptor species are significantly different chemical structures, the *g*-factors for the anion and cation are usually significantly different such that the anti-phase doublet associated with each radical can be resolved, giving rise to either an *a/e/a/e* or *e/a/e/a* polarization pattern, when these peaks are well separated. In our case the donor and acceptor systems are chemically identical and electron transfer occurs between two nearby PDI molecules which most likely have a δ^-/δ^+ type characteristic due to small local differences, resulting in very little structure in the trEPR signal apart from an overall narrow absorptive/emissive state which clearly indicates a CT state. The increase in the CT state signal relative to the triplet state signal with decreasing temperature and the increasingly symmetric *a/e* pattern would suggest that there are either small changes in conformation or changes in the competing photo-physical process making charge transfer the preferred pathway at lower temperatures. As however the increase in the CT state signal is much larger in PDI₂ compared to PDI₅, we would assume that the PDI₂ structure is more flexible and depends on temperature, however further works is needed before confirming the exact changes with temperature between all three PDI/DNA constructs both in the CT state and triplet state dynamics and yields. The trEPR analysis of the PDI/DNA series illustrates how the DNA-encoded assembly allows for fine tuning of the triplet and CT state formation mechanisms. These insights will be transferable to other molecular semiconductors, enabling for example the fine-tuning of constructs for singlet fission.

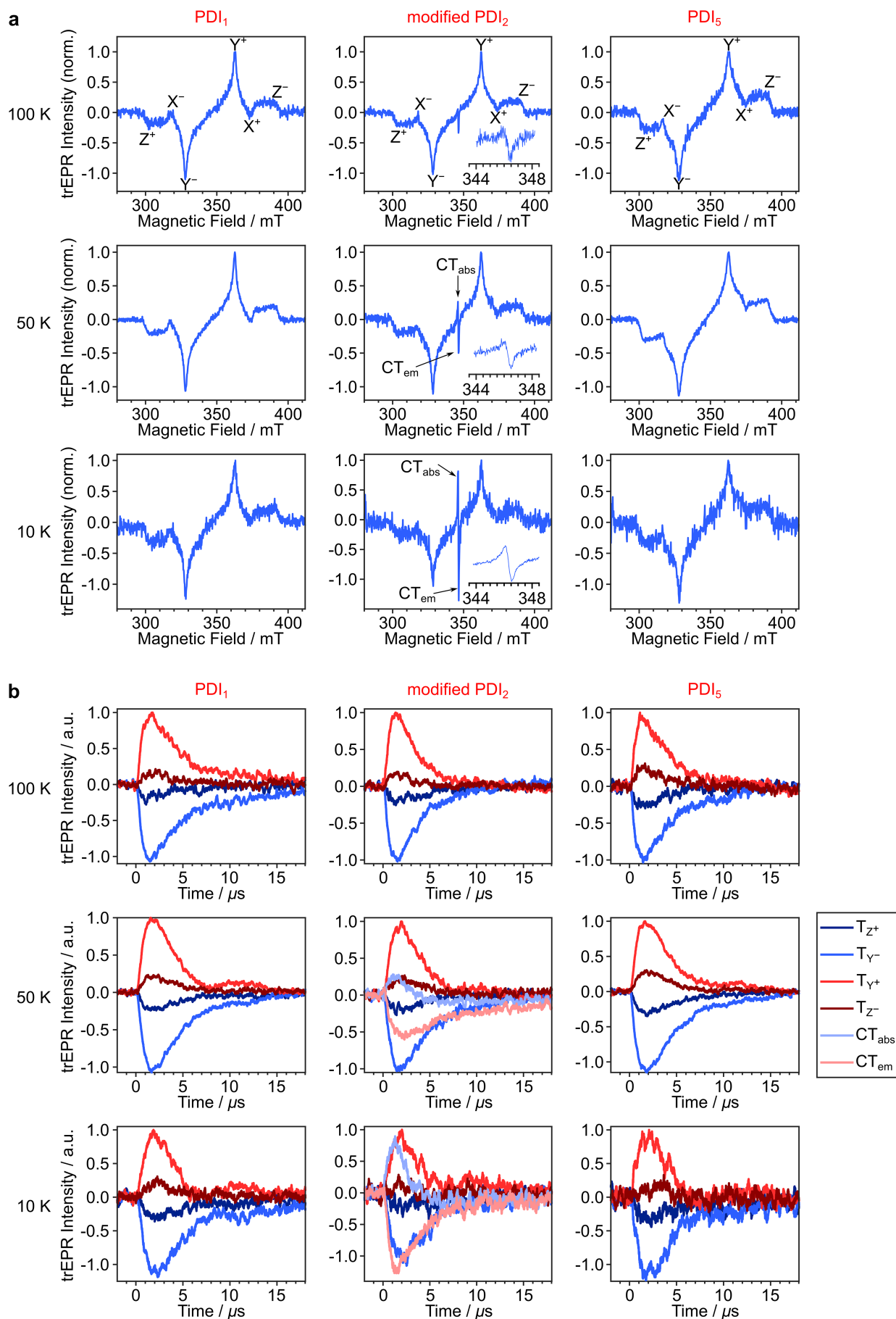


Figure S14-1. (a) trEPR spectra taken for **PDI₁**, modified **PDI₂** and **PDI₅** at 100 K, 50 K and 10 K after 532 nm excitation. Microwave power is 7.9 μW, DAF = 1.5 μs. Inset bottom right is the magnified CT state signal. (b) Transients taken at different magnetic field positions probing the time evolution of the triplet (all three samples) and, additionally, the CT state (**PDI₂**).

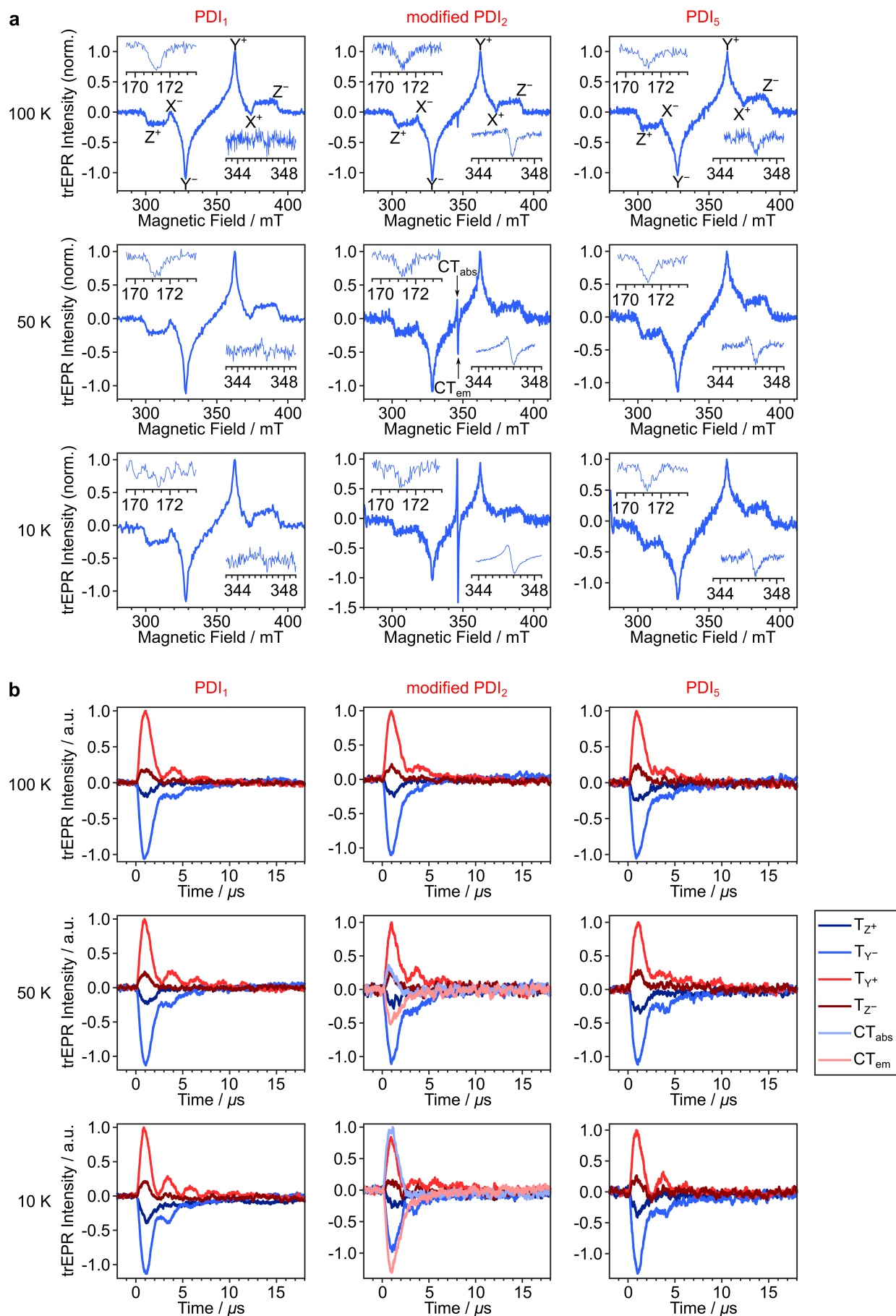
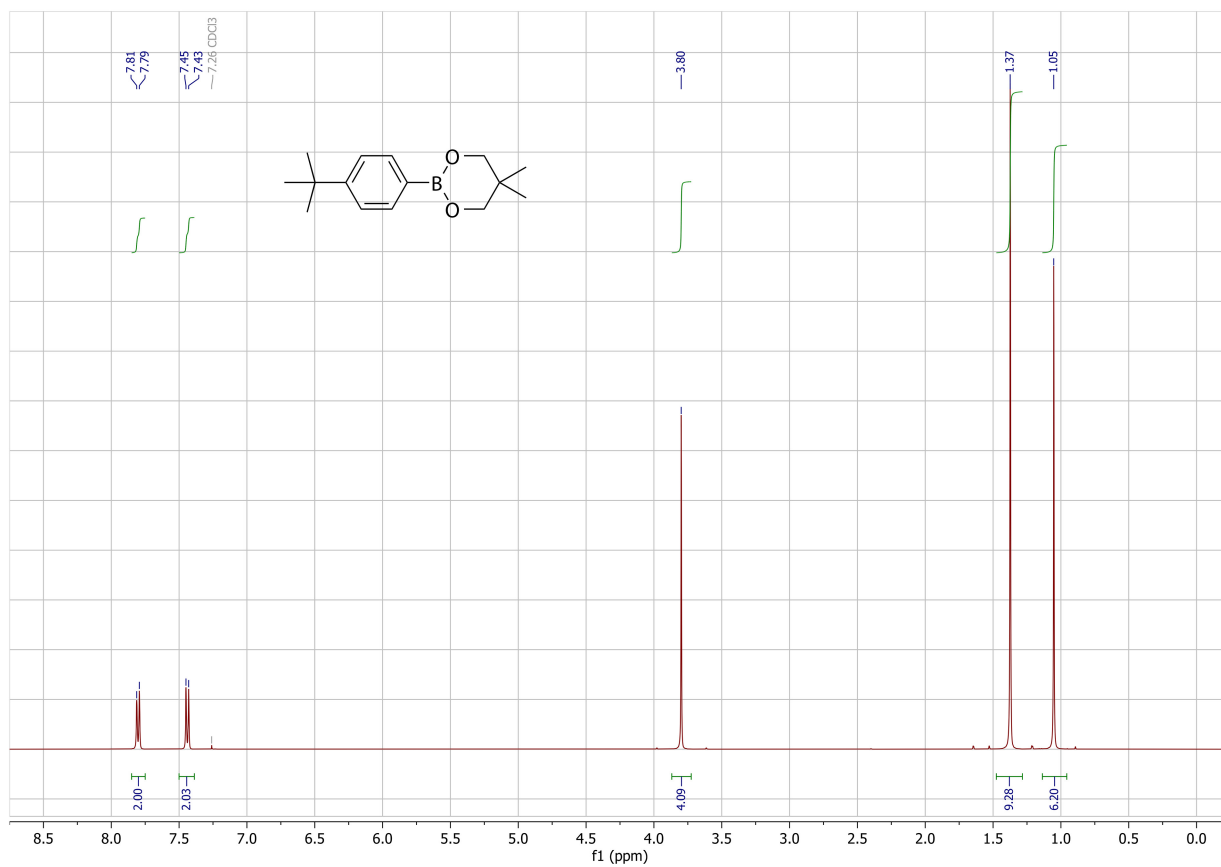
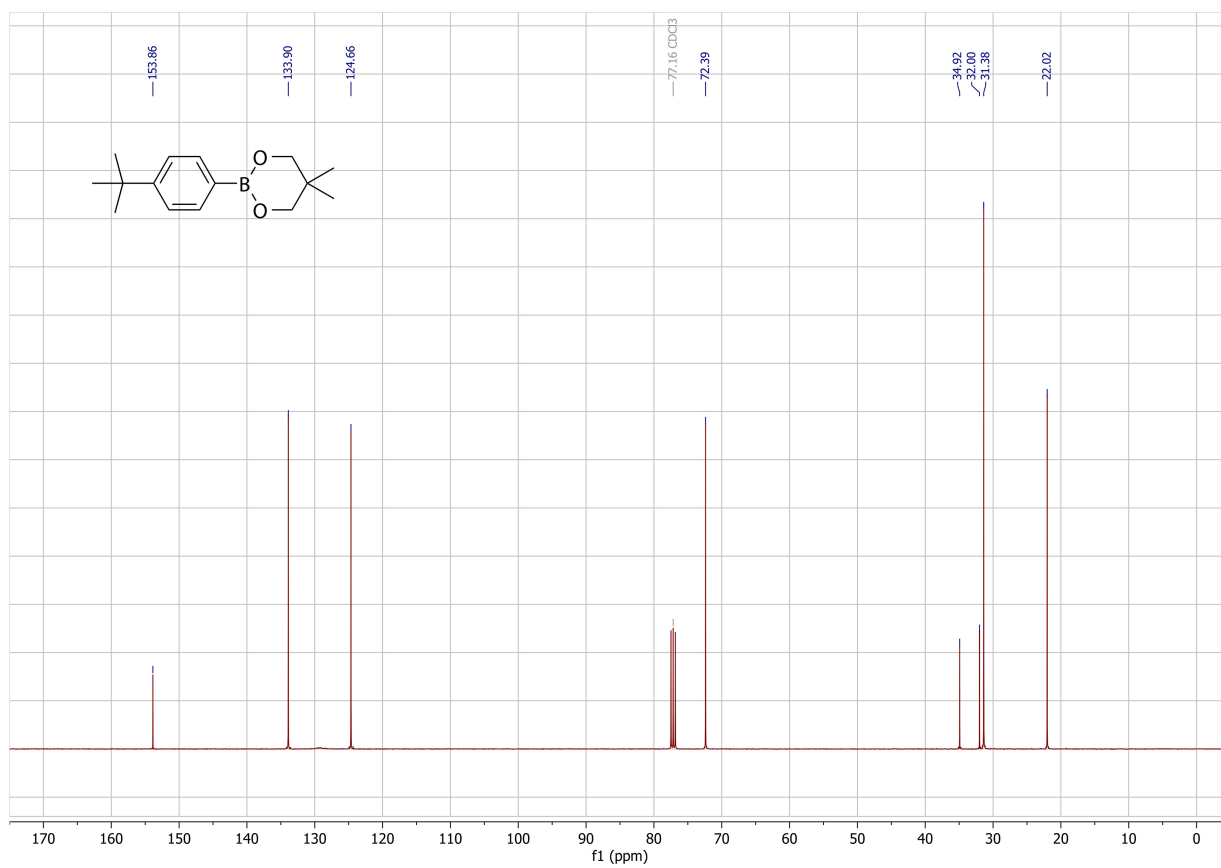


Figure S14-2. (a) trEPR spectra taken for **PDI₁**, the modified **PDI₂** and **PDI₅** at 100 K, 50 K and 10 K after 532 nm excitation. Microwave power is 126 μW, DAF = 0.9 μs. Inset top left is the half-field triplet state transition $\Delta m_s = \pm 2$, time averaged 0.3 – 2 μs. Inset bottom right is the magnified CT state spectrum. (b) Transients taken at different magnetic field positions probing the time evolution of the triplet (all three samples) and, additionally, the CT state (**PDI₂**).

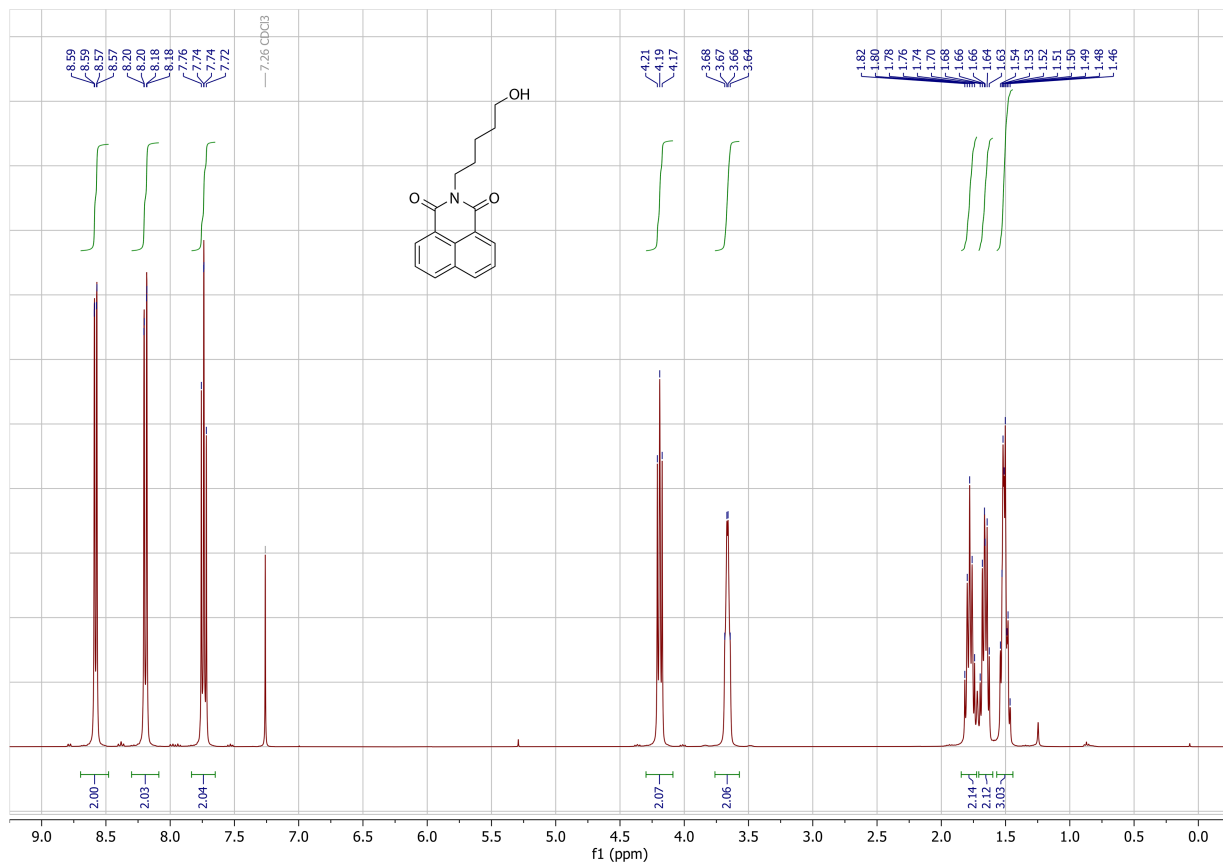
N. NMR spectra



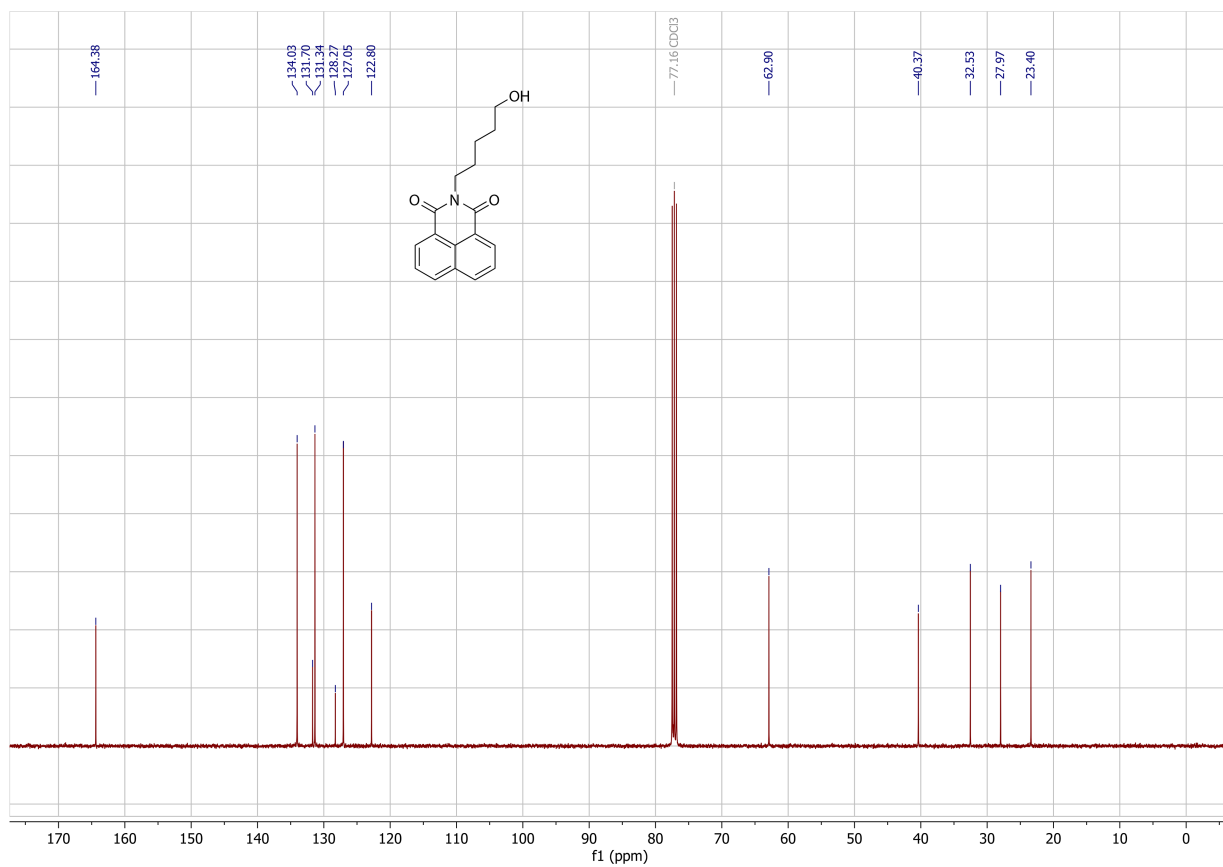
¹H NMR spectrum of the 4-*tert*-butylphenylboronic acid neopentyl glycol ester.



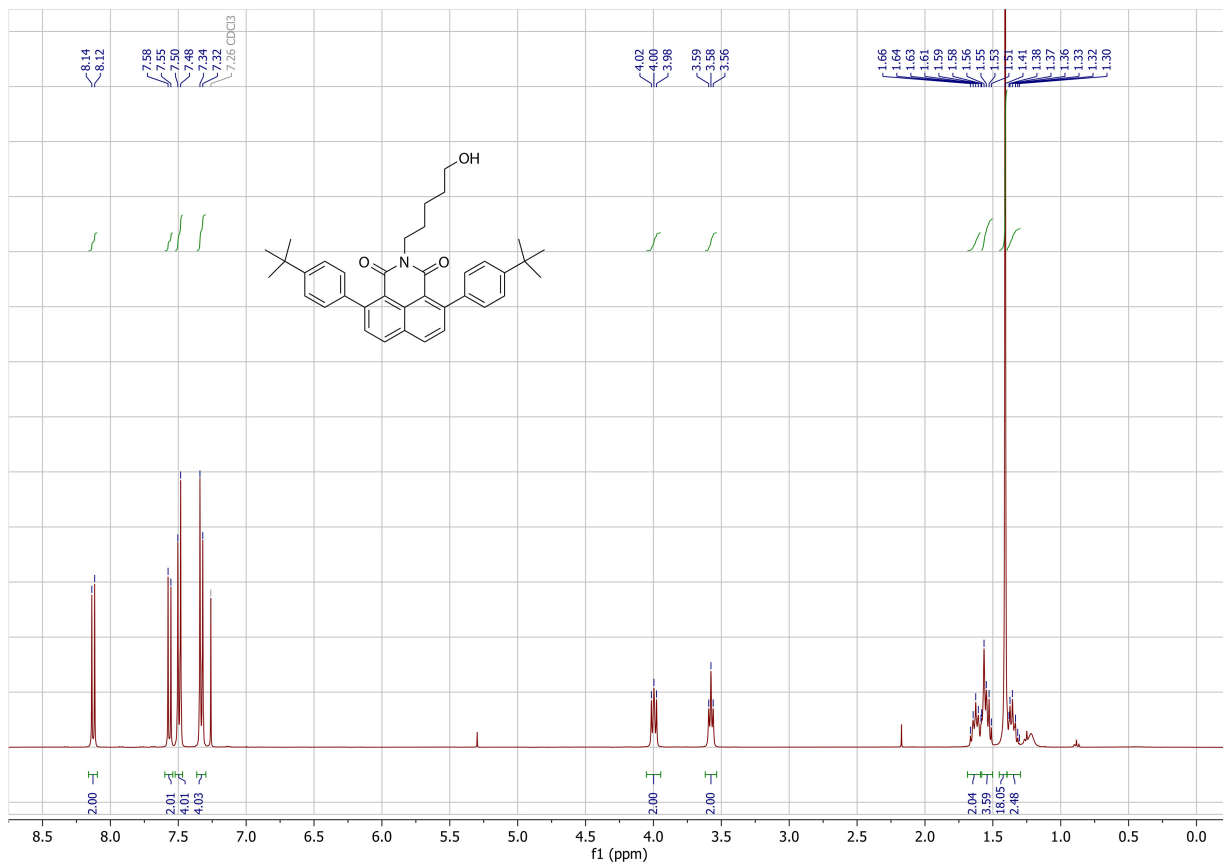
¹³C NMR spectrum of the 4-*tert*-butylphenylboronic acid neopentyl glycol ester.



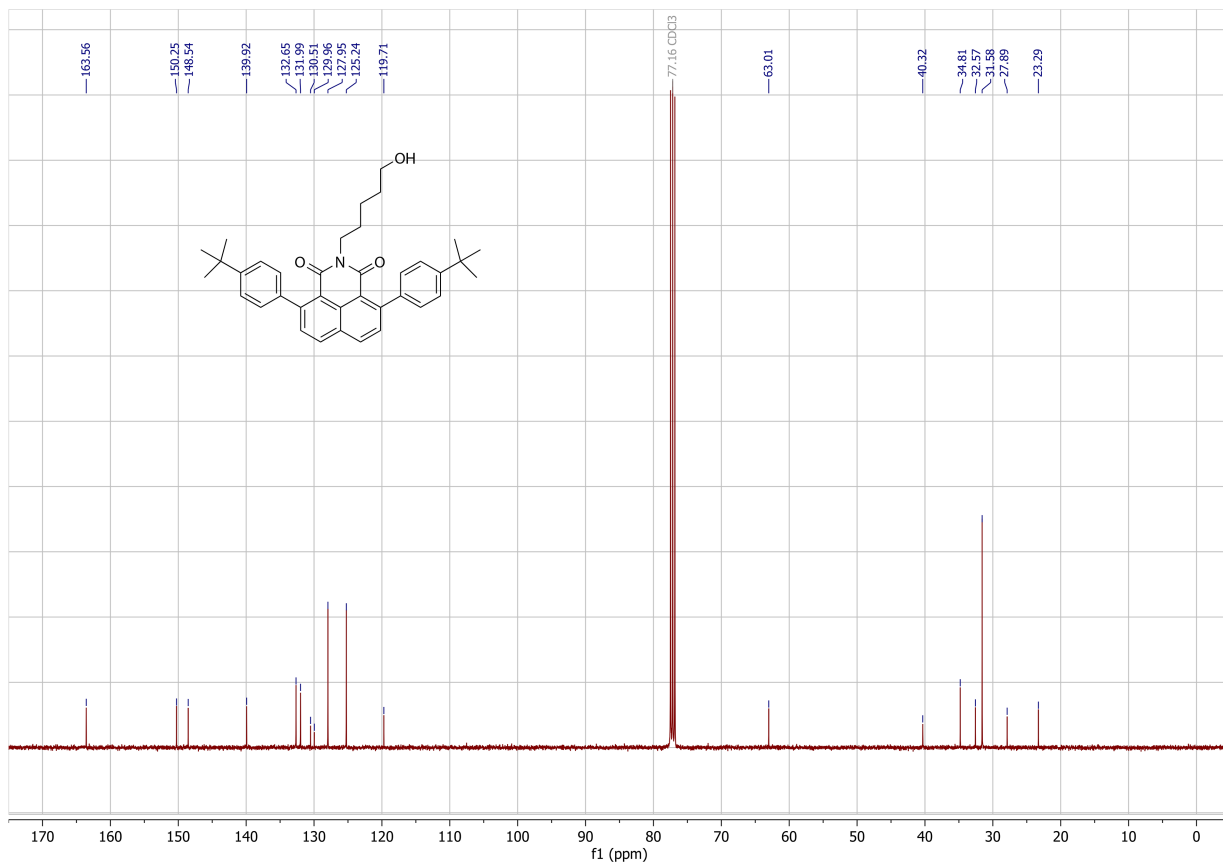
¹H NMR spectrum of compound 1.



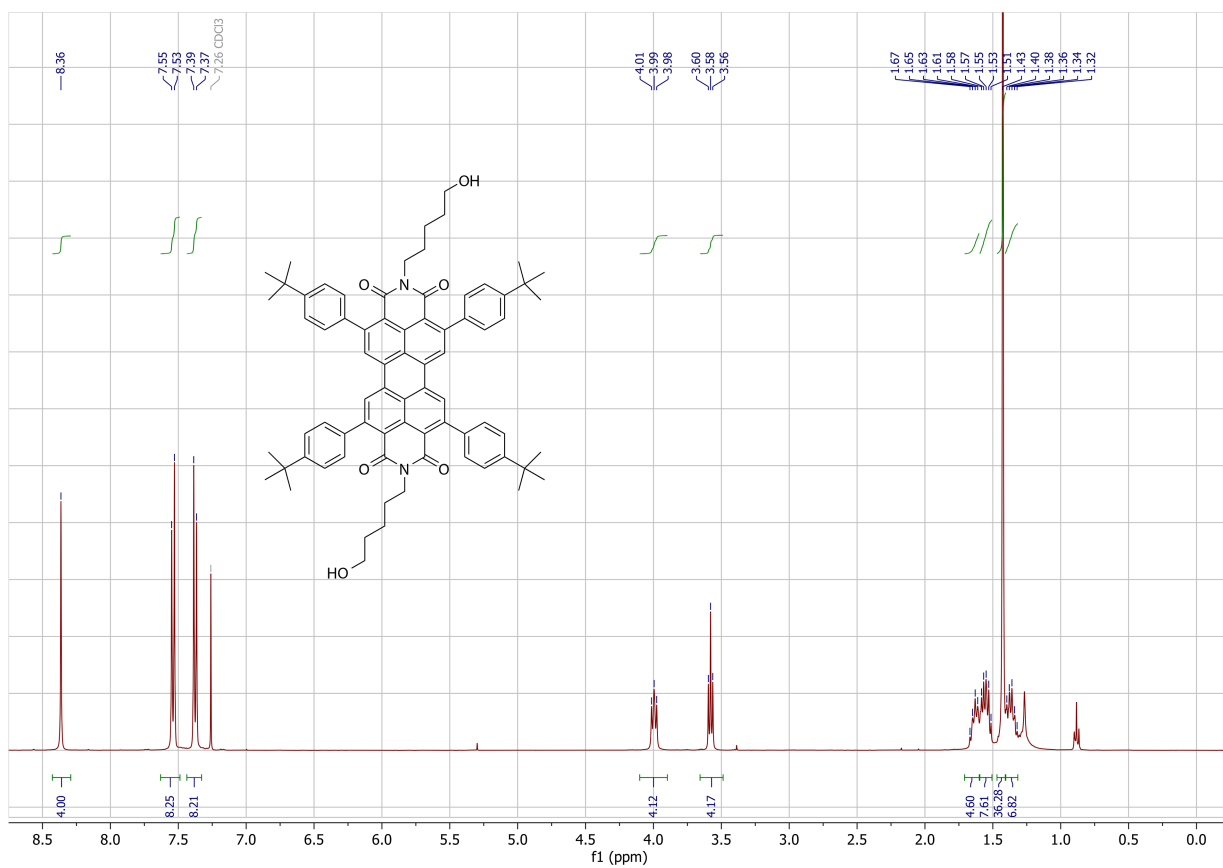
¹³C NMR spectrum of compound 1.



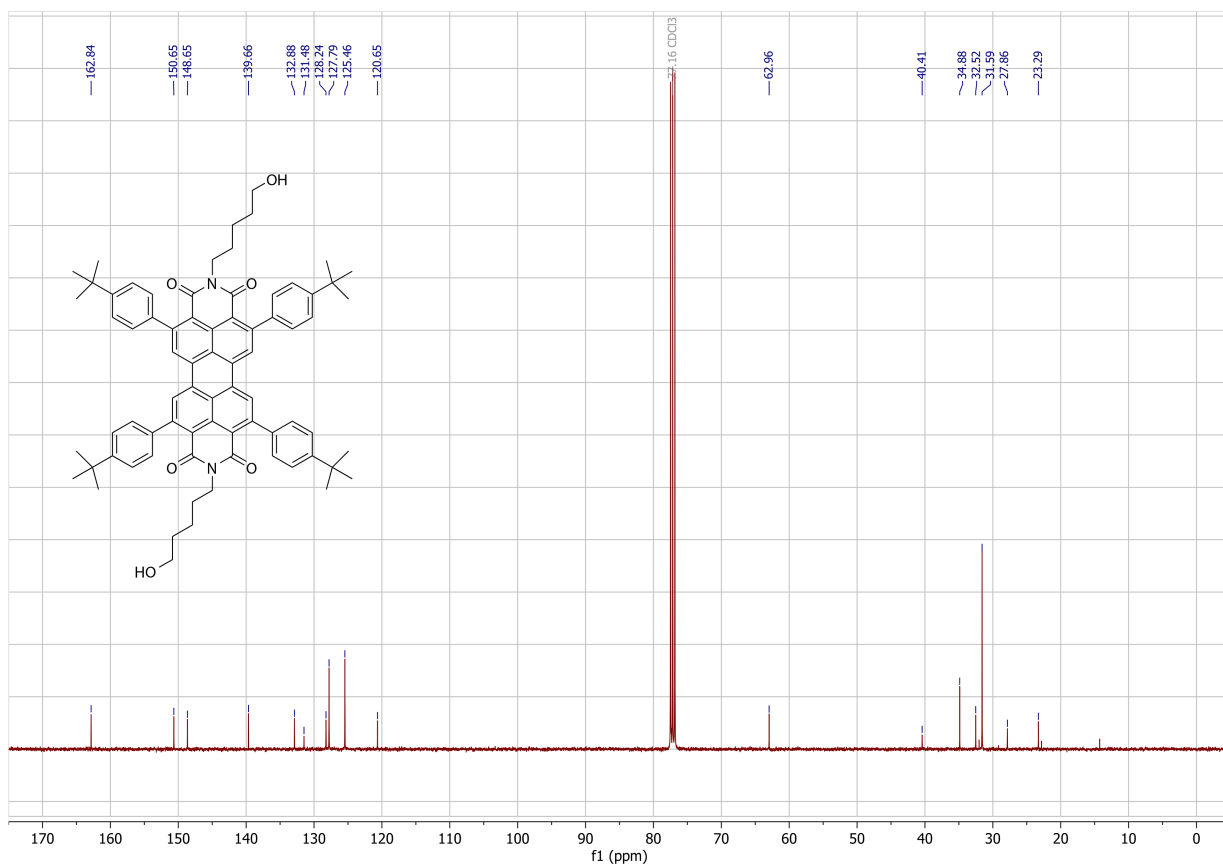
¹H NMR spectrum of compound 2.



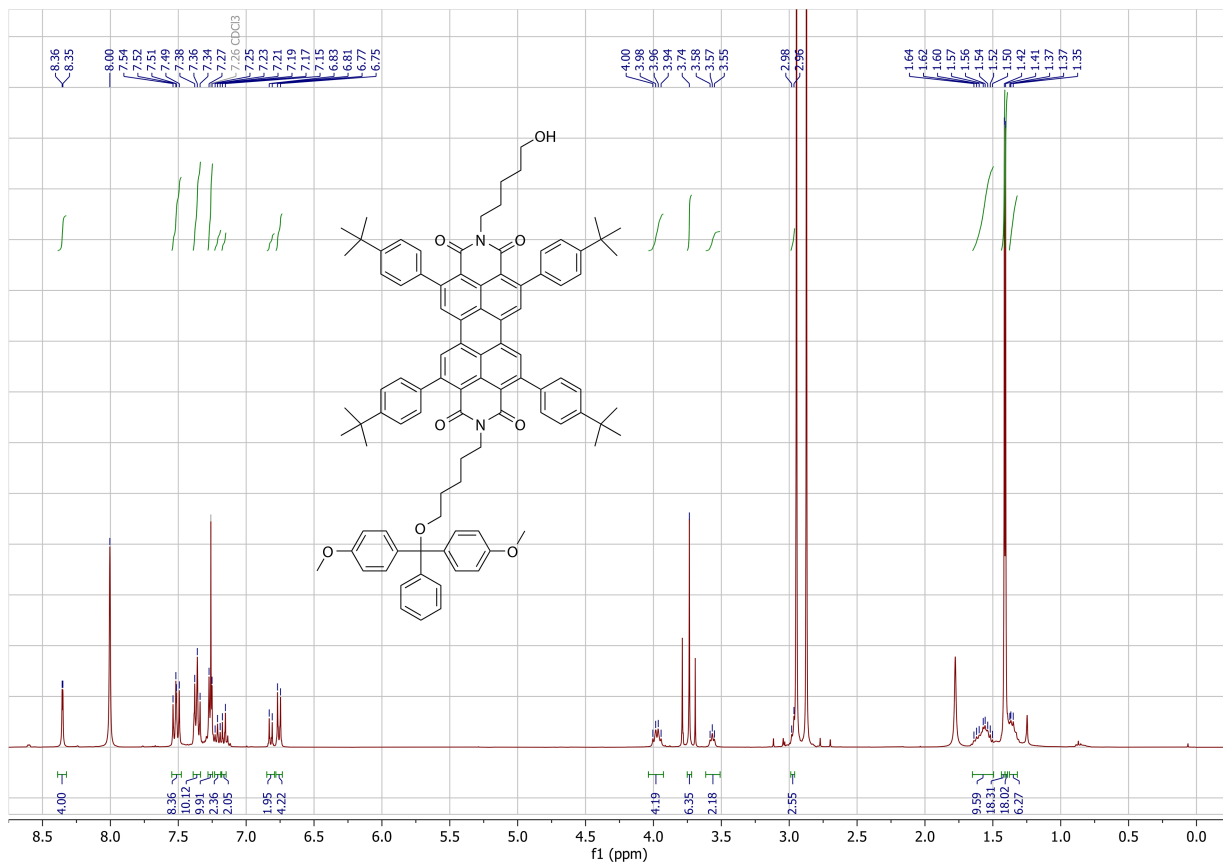
¹³C NMR spectrum of compound 2.



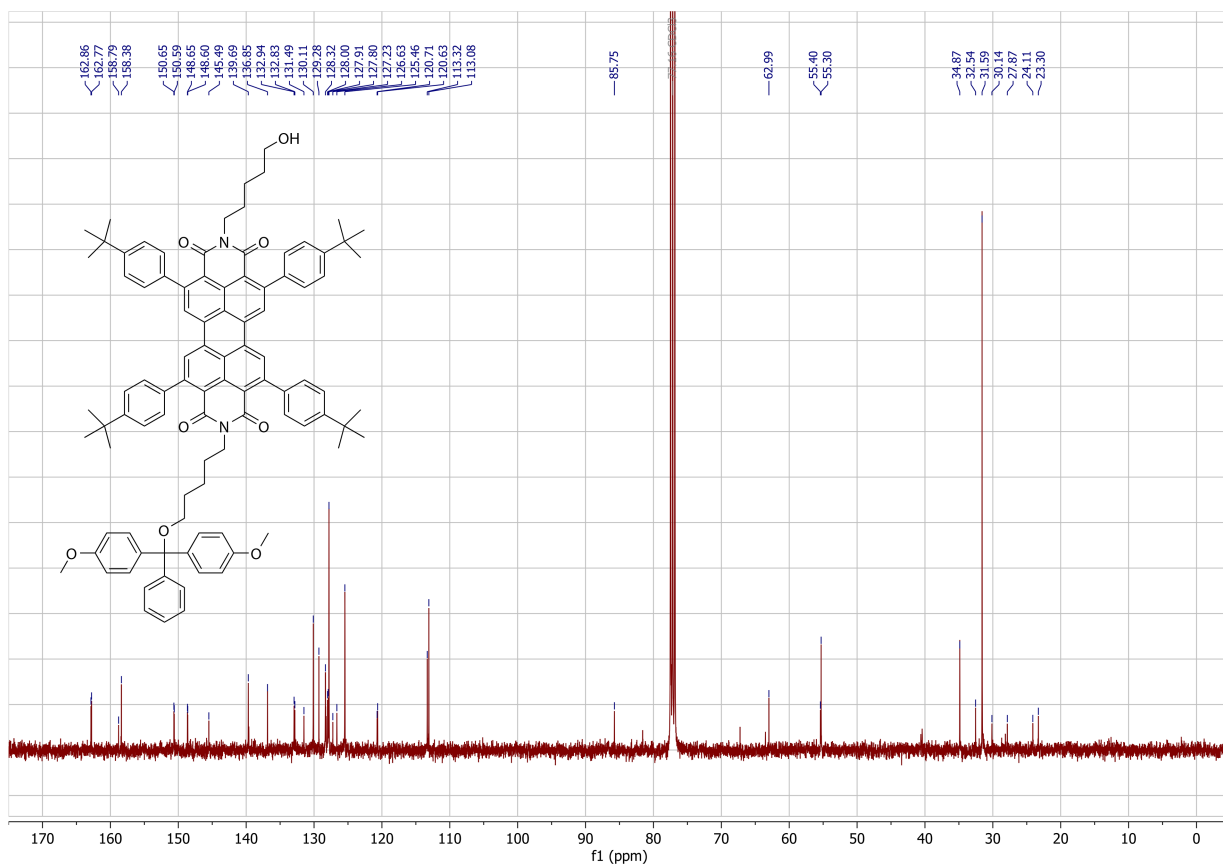
¹H NMR spectrum of compound 3.



¹³C NMR spectrum of compound 3.



¹H NMR spectrum of compound 4.



¹³C NMR spectrum of compound 4.

O. References

- [1] J. C. de Mello, H. F. Wittmann, R. H. Friend, *Adv. Mater.* **1997**, *9*, 230.
- [2] F. Neese, *WIREs Comput. Mol. Sci.* **2012**, *2*, 73.
- [3] F. Neese, *WIREs Comput. Mol. Sci.* **2018**, *8*, e1327.
- [4] T. Yanai, D. P. Tew, N. C. Handy, *Chem. Phys. Lett.* **2004**, *393*, 51.
- [5] F. Weigend, R. Ahlrichs, *Phys. Chem. Chem. Phys.* **2005**, *7*, 3297.
- [6] M. E. Madjet, A. Abdurahman, T. Renger, *J. Phys. Chem. B* **2006**, *110*, 17268.
- [7] J. Zhang, *J. Chem. Theory Comput.* **2018**, *14*, 572.
- [8] T. Lu, F. Chen, *J. Comput. Chem.* **2012**, *33*, 580.
- [9] S. Stoll, A. Schweiger, *J. Magn. Reson.* **2006**, *178*, 42.
- [10] T. L. Andersen, M. W. Frederiksen, K. Domino, T. Skrydstrup, *Angew. Chem. Int. Ed.* **2016**, *55*, 10396.
- [11] S. Singha Roy, P. Ghosh, U. H. Sk, P. Chakraborty, J. Biswas, S. Mandal, A. Bhattacharjee, S. Bhattacharya, *Bioorg. Med. Chem. Lett.* **2010**, *20*, 6951.
- [12] S. Nakazono, S. Easwaramoorthi, D. Kim, H. Shinokubo, A. Osuka, *Org. Lett.* **2009**, *11*, 5426.
- [13] T. Sakamoto, C. Pac, *J. Org. Chem.* **2001**, *8*, 94.
- [14] E. F. Pettersen, T. D. Goddard, C. C. Huang, G. S. Couch, D. M. Greenblatt, E. C. Meng, T. E. Ferrin, *J. Comput. Chem.* **2004**, *25*, 1605.
- [15] E. Vanquelef, S. Simon, G. Marquant, E. Garcia, G. Klimerak, J. C. Delepine, P. Cieplak, F.-Y. Dupradeau, *Nucleic Acids Res.* **2011**, W511.
- [16] C. I. Bayly, P. Cieplak, W. Cornell, P. A. Kollman, *J. Phys. Chem.* **1993**, *97*, 10269.
- [17] V. Hornak, R. Abel, A. Okur, B. Strockbine, A. Roitberg, C. Simmerling, *Proteins Struct. Funct. Bioinforma.* **2006**, *65*, 712.
- [18] K. Lindorff-Larsen, S. Piana, K. Palmo, P. Maragakis, J. L. Klepeis, R. O. Dror, D. E. Shaw, *Proteins Struct. Funct. Bioinforma.* **2010**, *78*, 1950.
- [19] I. Ivani, P. D. Dans, A. Noy, A. Pérez, I. Faustino, A. Hospital, J. Walther, P. Andrio, R. Goñi, A. Balaceanu, G. Portella, F. Battistini, J. L. Gelpí, C. González, M. Vendruscolo, C. A. Lughton, S. A. Harris, D. A. Case, M. Orozco, *Nat. Methods* **2016**, *13*, 55.
- [20] J. Wang, W. Wang, P. A. Kollman, D. A. Case, *J. Mol. Graph. Model.* **2006**, *25*, 247.
- [21] J. Wang, R. M. Wolf, J. W. Caldwell, P. A. Kollman, D. A. Case, *J. Comput. Chem.* **2004**, *25*, 1157.
- [22] M. D. Hanwell, D. E. Curtis, D. C. Lonie, T. Vandermeersch, E. Zurek, G. R. Hutchison, *J. Cheminform.* **2012**, *4*, 17.
- [23] D. A. Case, T. E. Cheatham III, T. Darden, H. Gohlke, R. Luo, K. M. Merz Jr., A. Onufriev, C. Simmerling, B. Wang, R. J. Woods, *J. Comput. Chem.* **2005**, *26*, 1668.
- [24] W. L. Jorgensen, J. Chandrasekhar, J. D. Madura, *J. Chem. Phys.* **1983**, *79*, 926.
- [25] I. S. Joung, T. E. Cheatham, *J. Phys. Chem. B* **2008**, *112*, 9020.
- [26] M. J. Abraham, T. Murtola, R. Schulz, S. Páll, J. C. Smith, B. Hess, E. Lindahl, *SoftwareX* **2015**, *1*, 19.
- [27] M. R. Shirts, C. Klein, J. M. Swails, J. Yin, M. K. Gilson, D. L. Mobley, D. A. Case, E. D. Zhong, *J. Comput. Aided Mol. Des.* **2017**, *31*, 147.
- [28] G. Bussi, D. Donadio, M. Parrinello, *J. Chem. Phys.* **2007**, *126*, 014101.
- [29] M. Parrinello, *J. Appl. Phys.* **1981**, *52*, 7182.
- [30] T. Darden, D. York, L. Pedersen, *J. Chem. Phys.* **1993**, *98*, 10089.
- [31] M. Bonomi, D. Branduardi, G. Bussi, C. Camilloni, D. Provasi, P. Raiteri, D. Donadio, F. Marinelli, F. Pietrucci, R. A. Broglia, M. Parrinello, *Comput. Phys. Commun.* **2009**, *180*, 1961.
- [32] G. A. Tribello, M. Bonomi, D. Branduardi, C. Camilloni, G. Bussi, *Comput. Phys. Commun.* **2014**, *185*, 604.
- [33] N. Michaud-Agrawal, E. J. Denning, T. B. Woolf, O. Beckstein, *J. Comput. Chem.* **2011**, *32*, 2319.
- [34] A. Laio, M. Parrinello, *Proc. Nat. Acad. Sci. USA* **2002**, *99*, 12562.
- [35] A. Barducci, G. Bussi, M. Parrinello, *Phys. Rev. Lett.* **2008**, *100*, 020603.
- [36] S. Piana, A. Laio, *J. Phys. Chem. B* **2007**, *111*, 4553.

- [37] A. Sridhar, S. E. Farr, G. Portella, T. Schlick, M. Orozco, R. Collepardo-Guevara, *Proc. Natl. Acad. Sci. USA* **2020**, *117*, 7216.
- [38] S. W. Eaton, L. E. Shoer, S. D. Karlen, S. M. Dyar, E. A. Margulies, B. S. Veldkamp, C. Ramanan, D. A. Hartzler, S. Savikhin, T. J. Marks, M. R. Wasielewski, *J. Am. Chem. Soc.* **2013**, *135*, 14701.
- [39] Z. Yu, Y. Wu, Q. Peng, C. Sun, J. Chen, J. Yao, H. Fu, *Chem. Eur. J.* **2016**, *22*, 4717.
- [40] L. E. Shoer, S. W. Eaton, E. A. Margulies, M. R. Wasielewski, *J. Phys. Chem. B* **2015**, *119*, 7635.
- [41] B. Gao, H. Li, H. Liu, L. Zhang, Q. Bai, X. Ba, *Chem. Commun.* **2011**, *47*, 3894.
- [42] W. Yang, J. Zhao, C. Sonn, D. Escudero, A. Karatay, H. G. Yaglioglu, B. I. Küçüköz, M. Hayvali, C. Li, D. Jacquemin, *J. Phys. Chem. C* **2016**, *120*, 10162.
- [43] P. P. Neelakandan, T. A. Zeidan, M. McCullagh, G. C. Schatz, J. Vura-Weis, C. H. Kim, M. R. Wasielewski, F. D. Lewis, *Chem. Sci.* **2014**, *5*, 973.
- [44] R. Carmieli, T. A. Zeidan, R. F. Kelley, Q. Mi, F. D. Lewis, M. R. Wasielewski, *J. Phys. Chem. A* **2009**, *113*, 4691.
- [45] M. Hariharan, Y. Zheng, H. Long, T. A. Zeidan, G. C. Schatz, J. Vura-Weis, M. R. Wasielewski, X. Zuo, D. M. Tiede, F. D. Lewis, *J. Am. Chem. Soc.* **2009**, *131*, 5920.
- [46] T. M. Wilson, T. A. Zeidan, M. Hariharan, F. D. Lewis, M. R. Wasielewski, *Angew. Chem. Int. Ed.* **2010**, *49*, 2385.
- [47] T. Takada, A. Ashida, M. Nakamura, M. Fujitsuka, T. Majima, K. Yamana, *J. Am. Chem. Soc.* **2014**, *136*, 6814.
- [48] R. E. Cook, B. T. Phelan, R. J. Kamire, M. B. Majewski, R. M. Young, M. R. Wasielewski, *J. Phys. Chem. A* **2017**, *121*, 1607.
- [49] Z. E. X. Dance, S. M. Mickley, T. M. Wilson, A. Butler Ricks, A. M. Scott, M. A. Ratner, M. R. Wasielewski, *J. Phys. Chem. A* **2008**, *112*, 4194.
- [50] H. van Willigen, G. Jones, M. S. Farahat, *J. Phys. Chem.* **1996**, *100*, 3312.
- [51] T. Okada, I. Karaki, E. Matsuzawa, N. Mataga, Y. Sakata, S. Misumi, *J. Phys. Chem.* **1981**, *85*, 3957.
- [52] T. Miura, R. Carmieli, M. R. Wasielewski, *J. Phys. Chem. A* **2010**, *114*, 5769.
- [53] G. L. Closs, M. D. E. Forbes, J. R. Norris, *J. Phys. Chem.* **1987**, *91*, 3592.
- [54] J. R. Norris, A. L. Morris, M. C. Thurnauer, J. Tang, *J. Chem. Phys.* **1990**, *92*, 4239.
- [55] P. J. Hore, D. A. Hunter, C. D. McKie, A. J. Hoff, *Chem. Phys. Lett.* **1987**, *137*, 495.